Metamorphism of Dolomitic and Magnesitic Rocks in Collisional Orogens and Implications for Orogenic CO_2 Degassing

Shashi Tamang[1,2], Chiara Groppo[1,3,*], Frédéric Girault[2], Frédéric Perrier[2] and Franco Rolfo[1,3]

[1]Department of Earth Sciences, University of Torino, 10125 Torino, Italy
[2]Institut de Physique du Globe de Paris, CNRS, Université Paris Cité, F-75005 Paris, France
[3]CNR-IGG, 10125 Torino, Italy

*Corresponding author. Telephone: +39 0116705106. E-mail: chiara.groppo@unito.it

Carbonate-bearing sediments, containing calcite, dolomite or magnesite as major carbonate components, are important constituents of sedimentary sequences deposited on passive margins through Earth's history. When involved in collisional orogenic processes, these sediments are metamorphosed at variable temperatures and pressures, and undergo decarbonation reactions. While the orogenic metamorphism of some of these lithologies (i.e. impure limestones and dolostones, marls *sensu stricto* and calcareous pelites) is relatively well understood, very little is known about the metamorphic evolution and decarbonation history of mixed carbonate–silicate rocks in which either dolomite or magnesite is the dominant carbonate component.

Here we present the results of a petrologic study of representative samples of metasediments from Central Nepal, derived from Proterozoic dolomitic and magnesitic protoliths metamorphosed during the Himalayan orogeny. The main metamorphic assemblages developed in sediments originally containing different amounts of dolomite or magnesite are characterised in detail. Forward thermodynamic modelling applied to seven samples allows constraints to be placed on (i) the main decarbonation reactions, (ii) the P–T conditions under which these reactions took place, (iii) the composition of the fluids, and (iv) the amounts of CO_2 released.

We conclude that the CO_2 productivity of dolomitic and magnesitic pelites and marls originally containing 15–40% carbonate is significant ($>5.5 \pm 1.0$ CO_2 wt% and up to 10.5 ± 1.5 CO_2 wt%), whereas for carbonate contents above 60–70%, CO_2 productivity is negligible unless aqueous fluids infiltrate from the outside and trigger decarbonation reactions. Since the dolomitic and magnesitic protoliths are significantly abundant in the sedimentary sequences involved in the still active Himalayan orogen, the decarbonation processes described here could contribute to the diffuse CO_2 degassing currently observed at the surface. Furthermore, we propose for the first time that the peculiar magnesium-rich assemblages investigated in this study may derive from evaporitic protoliths, and that the whole Upper Lesser Himalayan Sequence may therefore represent the metamorphic product of a Proterozoic sequence consisting of alternating layers of carbonatic, evaporitic and pelitic sediments.

Key words: CO_2 production; decarbonation processes; dolomite and magnesite; evaporitic protoliths; orogenic metamorphism

INTRODUCTION

Sedimentation on passive continental margins is controlled throughout Earth's history by the balance between the supply of terrigenous and biogenic sediments (Frisch *et al.,* 2011). The proportion and composition of the siliciclastic and carbonatic components depend on the characteristics of the margins (e.g. high or low relief, distance from river systems) and the climate; carbonate production appears particularly favoured in shallow, warm, well-circulated waters, where thick carbonate platforms can eventually form. In warm climates, carbonate platforms are often characterised by the development of biohermal barriers along the shelf margin and a lagoon behind where evaporitic conditions can be established. In such an environment, the process of dolomitisation is common, involving the replacement of the original calcium carbonate by dolomite and the formation of thick sequences of dolostones. The formation of magnesite deposits is also possible, as documented by the occurrence of sparry magnesite deposits, mostly concentrated within Precambrian carbonate sequences, and interpreted as the products of dolomite

replacement by magnesite in an evaporitic environment (e.g. Pohl, 1990; Frank & Fielding, 2003).

Most sedimentary sequences originally deposited on passive margins are subsequently involved in collisional orogenic processes through the Wilson cycle, and thus undergo metamorphism at variable temperatures, pressures and depths. During orogenic metamorphism, carbonatic lithologies tend to decarbonate, producing CO_2-rich fluids (e.g. Stewart *et al.,* 2019, and references therein). Decarbonation is one of the mechanisms operating in the so-called long-term carbon cycle (Bickle, 1996), through which carbon is transferred from the solid Earth to the ocean–atmosphere system. Other mechanisms of CO_2 production, less relevant in orogenic settings, include (i) congruent carbonate dissolution (e.g. Frezzotti *et al.,* 2011; Ague & Nicolescu, 2014; Kelemen & Manning, 2015; Ferrando *et al.,* 2017; Maffeis *et al.,* 2021), (ii) carbonate melting (e.g. Poli, 2015; Thomson *et al.,* 2016) and (iii) oxidation of graphite by iron reduction during biotite melting in graphitic metapelites (Cesare *et al.,* 2005). Processes (i) and (ii) are especially relevant in subduction settings, while process (iii) is relevant in granulitic terranes; these processes will not be further

considered in this study. Once produced at depth, CO_2 can rise to the surface along fault and fracture networks and eventually be released into the atmosphere (e.g. Kerrick & Caldeira, 1998; Becker et al., 2008; Evans et al., 2008; Girault et al., 2014, 2018, 2023a, 2023b; Kelemen & Manning, 2015; Plank & Manning, 2019; Groppo et al., 2022). During their ascent towards the surface, the CO_2-rich fluids may interact with the hosting lithologies at variable depths, and CO_2 can be therefore re-sequestered in the form of carbonate or graphite, as documented by a number of studies mostly focused on subduction zones (Hansen et al., 2005; Beinlich et al., 2014; Falk & Kelemen, 2015; Menzel et al., 2018; Sieber et al., 2018; Consuma et al., 2020; Hu et al., 2021). On the other hand, it has been recently demonstrated that carbon re-sequestration is hampered if fluid immiscibility occurs at depth in collisional orogens, allowing a rapid ascent of the CO_2-rich fluids without interaction with the host rocks (Groppo et al., 2022). Rather than on the CO_2 mobility and transfer, this study focuses on the processes of CO_2 production at depth, whose knowledge is preliminary to further investigations of its mobility within the crust.

Decarbonation processes occurring in impure limestones and dolostones during orogenic metamorphism have been investigated in detail since the pioneering study by Bowen (1940), either in the very simple $CaO–MgO–SiO_2–H_2O–CO_2$ (CMS-HC) system (e.g. Goldsmith & Newton, 1969; Skippen, 1971, 1974; Skippen & Hutcheon, 1974; Moore & Kerrick, 1976; Baker et al., 1991) or considering the effects of additional components such as Al_2O_3, FeO or K_2O (e.g. Rice, 1977a, 1977b; Bowman & Essene, 1982; Carmichael, 1991; Castelli, 1991; Connolly & Trommsdorff, 1991; Schmädicke et al., 2001; Castelli et al., 2007; Groppo et al., 2007; Proyer et al., 2008). However, impure limestones and dolostones (i.e. rocks in which the amount of carbonates is greater than 50 vol%) represent only a small percentage of the carbonate-bearing protoliths deposited in the passive margin sedimentary sequences; instead, rocks consisting of a mixture of pelitic and carbonatic components are prevalent, ranging from marls and argillaceous marls (15–50 vol% carbonates) to carbonatic pelites (<15 vol% carbonates). Prograde metamorphic reactions occurring in some of these mixed carbonate–silicate rocks, such as marls *sensu stricto* (i.e. calcite-bearing marls) and calcareous pelites, are relatively well known (e.g. Hewitt, 1973; Thompson, 1975; Ferry, 1976, 1983a, 1983b, 1992; Zen, 1981; Harley & Buick, 1992; Dasgupta, 1993; Menard & Spear, 1993; Fitzsimons & Harley, 1994; Bhowmik et al., 1995; Cartwright et al., 1997; Sengupta et al., 1997; Stephenson & Cook, 1997; Mathavan & Fernando, 2001; Sengupta & Raith, 2002; Groppo et al., 2017, 2021, 2022; Rapa et al., 2017); these reactions generally involve the breakdown of calcite reacting with the silicate assemblage and the growth of calcium-rich minerals (e.g. plagioclase, zoisite, garnet, amphibole, clinopyroxene), the amount and composition of which depend on the amount of calcite originally present in the protolith, the bulk-rock composition and the pressure–temperature (P–T) metamorphic conditions.

Much less studied is the metamorphic evolution and decarbonation history of mixed carbonate–silicate rocks in which either dolomite or magnesite is the dominant carbonate component, i.e. dolomitic marls, dolomitic pelites, magnesitic marls and magnesitic pelites. This study aims at filling this gap of knowledge, focusing on metasediments derived from dolomitic and magnesitic protoliths exposed in the upper part of the Lesser Himalayan Sequence (LHS), Central Nepal, whose P–T evolution is constrained by data from the associated metapelites (Tamang et al., 2023). Compared to previous petrologic investigations on the decarbonation behaviour of carbonate metasediments from the

Himalayan belt (e.g. Kerrick & Caldeira, 1998; Groppo et al., 2017, 2021, 2022; Rapa et al., 2017), the novelties of this study especially concern the types of carbonate originally present in the protoliths (i.e. dolomite and magnesite vs. calcite) and the lithostratigraphic unit to which the samples studied belong (i.e. the Paleoproterozoic to Mesoproterozoic LHS vs. the Neoproterozoic Greater Himalayan Sequence [GHS]). The aim of the study is threefold: (i) to characterise the main assemblages and microstructures of metasediments derived from protoliths containing different amounts of dolomite or magnesite; (ii) to investigate the most relevant decarbonation reactions for each one of them; and (iii) to estimate the P–T conditions at which the decarbonation reactions took place, the composition of the fluids released by these reactions and the amounts of CO_2 released per unit volume of reacting rocks. Petrographic, bulk-rock and mineral chemistry data are used to address the first objective; the phase equilibrium modelling approach is used to address objectives (ii) and (iii). The importance of dolomitic and magnesitic metasediments as CO_2 sources in collisional orogens is discussed and compared with that of calcite-bearing metasediments from the literature, with potential implications for the estimation of the Earth's global CO_2 emission budget. Additional implications of this study, which represent a further novel insight with respect to previous studies, concern the interpretation of the depositional environment of the peculiar magnesium-rich lithologies here described.

GEOLOGICAL SETTING AND SAMPLES

The LHS is a thick metasedimentary sequence derived from the metamorphic transformation of the sediments deposited on the northern passive margin of the Indian Plate during the Proterozoic (e.g. Gansser, 1964; Parrish & Hodges, 1996; DeCelles et al., 2000; Martin et al., 2005). The LHS is tectonically sandwiched between the underlying Siwalik Group to the south and the overlying GHS to the north, from which it is separated by two major discontinuities, the Main Boundary Thrust and the Main Central Thrust (MCT), respectively (Yin & Harrison, 2000) (Fig. 1a). At the scale of the entire orogen, the LHS is exposed in the core of a broad antiform that develops longitudinally with respect to the Himalayan belt (i.e. the Lesser Himalayan Duplex: DeCelles et al., 2001; Pearson & DeCelles, 2005; Long & Robinson, 2021); this structural culmination has been more intensely eroded towards the west (Dhital, 2015), where the LHS is therefore more widely exposed. A well-known inverted metamorphism characterises the LHS, with the metamorphic grade increasing structurally upwards (and from south to north) from biotite to garnet, staurolite and kyanite first appearing (e.g. Pêcher, 1989; Kohn, 2014; Tamang et al., 2023).

The LHS is conventionally divided into two complexes (Fig. 1b) characterised by distinct lithological associations, which are representative of different depositional environments (Groppo et al., 2023, and references therein): the Lower-LHS (Lower Nawakot Unit; Stöcklin, 1980), dominated by siliciclastic rocks, and the Upper-LHS (Upper Nawakot Unit; Stöcklin, 1980), composed of both carbonate and siliciclastic rocks. U–Pb dating of detrital zircons constrains the depositional age of the Lower-LHS to the Paleo-Proterozoic, with most ages converging in the interval 1900–1850 Ma (Parrish & Hodges, 1996; DeCelles et al., 2000; Martin et al., 2005, 2011; Sakai et al., 2013), whereas the precise depositional age of the Upper-LHS sequence remains unconstrained, although a Meso-Proterozoic age has been tentatively proposed (e.g. DeCelles et al., 2001; Martin et al., 2005, 2011). Both units are intruded by Proterozoic igneous rocks, now mostly transformed into granitic
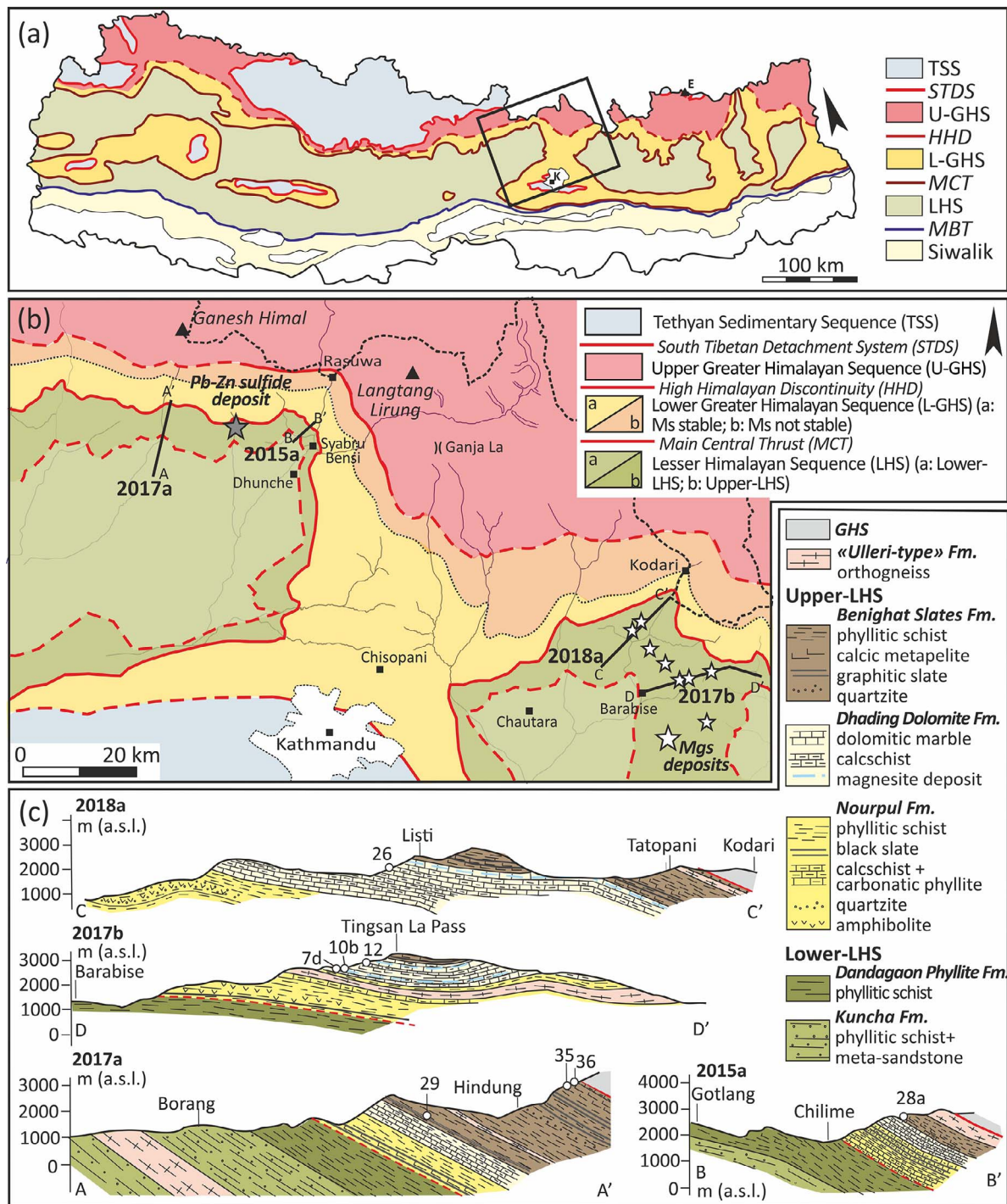
Fig. 1. (a) Geological sketch map of the Nepal Himalaya showing major tectono-metamorphic units (modified from Dhital, 2015). The black inset refers to the detailed map shown in (b). E: Everest; K: Kathmandu. (b) Geological sketch map of the central Nepal Himalaya, showing the location of the four sections from which the samples studied in detail were collected (black lines). Modified from Dhital (2015) and based on our own data. The grey and white stars indicate the location of the main Pb–Zn sulphide (grey) and magnesite (white) deposits. The dashed black line is the Nepal–China border. (c) Representative cross-sections across the Lower and Upper-LHS in central Nepal showing the location of the samples examined. The location of each section is given in (b).

augen gneisses (e.g. DeCelles *et al.,* 1998; Le Fort & Rai, 1999; Upreti, 1999; Kohn *et al.,* 2010) ('Ulleri-type' orthogneiss in Fig. 1c).

The samples analysed were collected in the Upper-LHS of Central Nepal (Fig. 1b). In this region, the following formations are exposed from the bottom to the top of the Upper-LHS sequence (Stöcklin, 1980; Upreti, 1999; Groppo *et al.,* 2023): Nourpul Formation, Dhading Dolomite Formation and Benighat Slates

Formation (Fig. 1c). The Nourpul Formation is a lithologically heterogeneous succession consisting of a thick intercalation of different types of metamorphic rocks derived from shale, marl and sandstone protoliths, i.e. phyllites, black slates, carbonatic phyllites, calcschists and minor quartzites. The Dhading Dolomite Formation overlies the Nourpul Formation with a transitional contact marked by a progressive increase in

carbonatic lithologies. It consists mainly of fine-grained dolomitic marbles with intercalations of calcschists, carbonatic phyllites and graphitic schists, respectively, derived from the metamorphic transformation of dolostones, dolomitic marls, dolomitic pelites and pelites enriched in carbonaceous material. Despite their metamorphic recrystallisation, the dolomitic marbles often retain features inherited from the protolith, including a finely laminated structure and remnants of stromatolitic structures (Supplementary Figs S1a–c). Veitsch-type magnesite deposits (i.e. hosted by marine carbonates; Pohl, 1990) are locally associated with the dolomitic rocks of the Dhading Dolomite Formation (Fig. 1b, c; Supplementary Figs S1d–h); magnesite has been interpreted as the syn-sedimentary diagenetic replacement of dolomite in an evaporitic environment that developed behind biohermal barriers that inhibited water circulation (Valdiya, 1995; Joshi & Sharma, 2015). Diagenetic features, such as radiating aggregates of coarse-grained magnesite in a fine-grained matrix ('rosettes': Pohl, 1990), are locally preserved in these deposits. The overlying Benighat Slates Formation is the thickest formation in the Upper-LHS. It is lithologically heterogeneous and is dominated by dark phyllites, with frequent intercalations of graphitic schists (e.g. Thapa *et al.*, 2023) and calcic metapelites, and minor carbonatic lithologies and quartzites (Supplementary Figs S1i–k). Protoliths of these lithologies are mostly represented by carbonaceous-rich pelites, dolomitic/magnesitic pelites and dolomitic/magnesitic marls, with minor dolostones and limestones.

Eight samples derived from the metamorphism of carbonatic protoliths were studied in detail. The samples were collected from four different cross-sections in Central Nepal (Fig. 1b, c), specifically selected because metapelitic rocks exposed along them have already been investigated (Tamang *et al.*, 2023), allowing constraints to be placed on the P–T evolution of the Upper-LHS in this area. The first two sections are located c. 50 km NNW of Kathmandu, in the upper part of the Ankhu valley (samples 17a-) c. 15 km NW of Dhunche, and in the upper part of the Trisuli valley (samples 15a-) c. 8 km north of Dhunche. The other two sections are located c. 60 km ENE of Kathmandu, in the upper part of the Sunkhosi valley along the Arniko highway (samples 18a-) and along the Barabise-Tinsang La section (samples 17b-). Samples 15a-28a, 17a-29, 17a-35 and 17a-36b belong to the Benighat Slates Formation, while samples 17b-7d, 17b-10b, 17b-12 and 18a-26 belong to the Dhading Dolomite Formation.

METHODS
Microstructures and mineral chemistry

For all the samples, high-resolution multispectral mapping was performed on the whole thin sections (c. 3 cm × 1.5 cm) to obtain their precise modal compositions and to highlight their microstructures at large scale. These X-ray maps were obtained using a JEOL IT300LV scanning electron microscope (SEM), USA, at the Dipartimento di Scienze della Terra, University of Torino, Italy. The instrument is equipped with an Energy 200 energy dispersive spectrometry (EDS) and an X-Act3 silicon drift detector (Oxford Inca Energy, UK). The operating conditions used for mapping are 15-kV acceleration voltage, process time 1, 2.5-μm spot size and 500-ms pixel dwell time. Raw data were processed using MultiSpec© software (Purdue Research Foundation, USA) to obtain the modal compositions.

Samples containing significant amounts of carbonate were additionally observed using the cathodoluminescence (CL) technique. CL images of the whole thin sections were obtained using the Cathodyne® CATHODO SP02 optical CL device (NewTec Scien-

tific, France) at the Institut de Physique du Globe de Paris (IPGP), Paris, France. The samples were analysed using the Cathodyne® software, with the current and voltage set at 170 μA and 13 kV, respectively, with the long exposure time.

The rock-forming minerals were analysed with the same SEM-EDS instrument used for the high-resolution X-ray maps. The operating conditions are 15-kV acceleration voltage, 10-mm working distance, 2-μs process time and 15-s counting time. Quantitative SEM-EDS data were acquired and processed using the Microanalysis Suite Issue 12, INCA Suite version 4.01 (Oxford Inca Energy); natural oxides and silicates standards from Astimex Scientific Limited were used to calibrate the raw data; the $\Phi\rho Z$ correction (Pouchou & Pichoir, 1988) was applied. Dataset 1 in the Supplementary Material reports the full set of compositional data for all minerals analysed in each sample. Most analyses were recalculated using NORM computer software (Ulmer, 1986); structural formulae were calculated based on 12 oxygens for garnet, 11 oxygens for muscovite and biotite, 48 oxygens for staurolite, 8 oxygens for plagioclase, 28 oxygens for chlorite, 6 oxygens for dolomite, 3 oxygens for calcite and magnesite, and 11 oxygens for talc. Amphibole group minerals were normalised using WinAmphcal software (Yavuz, 2007).

Estimation of bulk-rock compositions

The bulk-rock compositions of each sample (Table 1) were calculated by combining the estimated mineral modes (Table 2) with mineral chemistry (see Dataset 1 in the Supplementary Material) and taking into account the molar volumes of each phase (details in Dataset 2 in the Supplementary Material). Zoning of plagioclase and garnet has been considered in those samples in which it is more pronounced, and the modal abundance of the zoned mineral is >3 vol%, i.e. plagioclase in sample 17b-12 and garnet in sample 17a-29; in such cases, core and rim compositions have been combined with their respective modal amounts. In all the other samples, average plagioclase and garnet compositions have been used. Additional bulk-rock compositions of metapelites and carbonatic lithologies from the LHS and GHS were used to discuss the nature of the samples investigated, i.e. to recognise the occurrence of dolomite, magnesite and calcite series (Fig. 2). These bulk-rock compositions refer to samples previously studied by Groppo *et al.* (2009, 2021), Rapa *et al.* (2016, 2017) and Tamang *et al.* (2023) or to our own unpublished data. Most of these compositions were obtained by inductively coupled plasma atomic emission spectrometry analysis by ALS Chemex, Vancouver, Canada, except where explicitly stated in the reference papers. Table S1 in the Supplementary Material lists the full set of bulk-rock compositions used, whereas Table 1 summarises the results for the eight samples investigated in detail in this study. Mineral abbreviations in the text, figures and tables are taken from Whitney & Evans (2010).

Reconstruction of the protolith assemblages

Based on the bulk-rock compositions, the mineralogical compositions of the protoliths (i.e. the modal proportions of the protolith minerals) were obtained (Table S2 in the Supplementary Material) using the least-squares method (PCalc; Godard, 2009) and using end-member compositions and molar volumes for kaolinite, illite, clinochlore, daphnite, albite, anorthite, quartz, K-feldspar, calcite, dolomite and magnesite. The result is considered satisfactory if the residuals (i.e. molar bulk composition of the protolith minerals minus molar bulk-rock composition) are close to zero. The reconstructed protolith assemblages are approximate, due to a number of assumptions that are required by the method itself.

Table 1: Bulk compositions (mol%) and protoliths' assemblages (vol%) of the studied samples from the Upper-LHS, Central Nepal Himalaya

	Dolomite series					Magnesite series		
	Dolomitic pelites		Dolomitic marls		Dolostone	Magnesitic pelite	Magnesitic marl	Magnesite ore
Sample	17b-12	17a-29	15a-28a	18a-26	17b-10b	17a-36b	17a-35	17b-7d
SiO_2	71.19	65.17	54.57	59.26	23.24	79.20	61.50	14.56
Al_2O_3	11.24	11.51	7.32	3.40	0.41	7.76	10.53	1.72
TiO_2	0.35	0.24	0.29	0.04	0.02	0.28	0.16	0.00
FeO	4.38	6.14	3.41	1.26	0.78	0.70	7.31	1.14
Fe_2O_3	0.49	0.00	0.00	0.00	0.00	0.67	0.00	0.00
MnO	0.03	0.32	0.03	0.00	0.00	0.00	0.01	0.00
MgO	5.24	8.36	16.77	19.52	37.31	8.06	18.26	82.42
CaO	3.26	6.04	15.27	15.39	37.69	0.15	1.13	0.16
Na_2O	1.03	0.50	0.38	0.53	0.00	0.33	0.20	0.00
K_2O	2.79	1.73	1.95	0.59	0.17	2.85	0.90	0.00
Kao	0	11	0	0	0	0	21	5
Ill	29	24	20	3	0	25	12	0
FeChl	8	10	6	2	1	2	12	2
MgChl	5	5	3	0	0	0	0	0
Qz	33	31	28	47	16	50	32	9
Ab	8	4	3	5	0	3	2	0
Kfs	7	0	4	0	1	10	0	0
An	4	2	1	2	0	1	1	0
Dol	6	14	36	41	80	0	2	0.4
Mgs	0	0	0	0	0	9	18	84
Cal	0	0	0	0	0.5	0	0	0
Ill/Cb	4.8	1.7	0.6	0.1	0.0	2.8	0.7	0.0

Table 2: Assemblages and modal compositions (vol%) of the studied samples from the Upper-LHS, Central Nepal Himalaya

	Dolomite series					Magnesite series		
	Dolomitic pelites		Dolomitic marls		Dolostone	Magnesitic pelite	Magnesitic marl	Magnesite ore
Sample	17b-12	17a-29	15a-28a	18a-26	17b-10b	17a-36b	17a-35	17b-7d
Cal	–	3	14	–	–	–	–	–
Dol	–	1	7	37	81	–	–	–
Mgs	–	–	–	–	–	–	–	74
Qz	37	36	26	42	16	54	27	–
Bt/Phl	23	18	32	8	2	21	20	–
Mu	17	8	–	–	–	24	–	–
Chl	–	6	–	4	–	–	–	14
Pl	21	18	10	8	–	2	–	–
Zo/Ep	<1		–	–	–	<1	–	–
Grt	2	7	–	–	–	–	3	–
Crd	–	–	–	–	–	–	5	–
Hbl	–	–	11	–	–	–	6	–
Oamp	–	–	–	–	–	–	29	–
Ky	–	2	–	1	–	–	10	–
St	–	1	–	–	–	–	–	–
Tlc	–	–	–	–	–	–	–	12

–, not observed.

The least-square algorithm, in fact, provides a unique solution (and null residual) when the number of independent equations (i.e. the number of components) is equal to the number of the unknowns (i.e. the number of the phase coefficients to be estimated). However, if the number of phases is greater than the number of components, the problem is underestimated, which means that an infinity of solutions exists. Some assumptions are thus required in order to maintain the number of phases in the protolith lower than (or equal to) the number of independent components. These assumptions include the following: (1) CaO from silicate fraction (CaO(silic) in Dataset 3 in the Supplementary Material) is equivalent to Na_2O and is incorporated into anorthite, while the remaining CaO (CaO(carb) in Dataset 3 in the Supplementary Material) is incorporated into calcite or dolomite; albite incorporates all Na_2O. This assumption is commonly applied in sedimentology for paleoenvironmental and provenance analyses (e.g. McLennan *et al.,* 1993; Hofer *et al.,* 2013). The strong negative correlation between CaO and Al_2O_3 observed in the studied
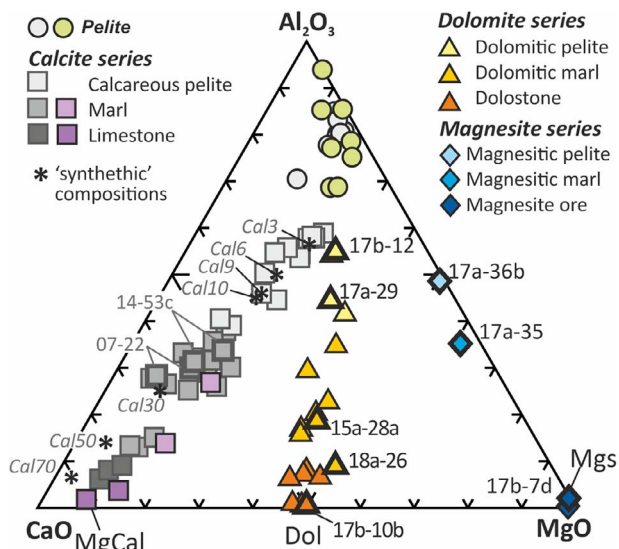
Fig. 2. Compositional variation of different types of carbonate-bearing lithologies and metapelites from the LHS (coloured symbols) and GHS (grey symbols), plotted in the CaO–Al$_2$O$_3$–MgO diagram. Samples belonging to the calcite, dolomite and magnesite series are aligned along three different trends defined by symbols from dark to light sqaures (calcite series), triangles (dolomite series) and from diamonds (magnesite series). Note that all samples analysed from the GHS (grey symbols) belong to the calcite series. Symbols with thick borders refer to samples whose CO$_2$ productivity was investigated either in this study or in previous publications (Groppo *et al.*, 2017; Rapa *et al.*, 2017). Asterisks refer to 'synthetic' compositions studied by Groppo *et al.* (2021) (Cal3, Cal6, Cal9) and Groppo *et al.* (2022) (Cal10, Cal30, Cal50, Cal70).

samples (Supplementary Fig. S3a) demonstrates that Ca is not influenced significantly by a detrital source (e.g. feldspars), but instead is nearly all of marine origin and justifies the use of Na$_2$O as a substitute for CaO(silic). (2) FeO enters only in chlorite rather than in ankerite and/or Fe-oxides and Fe-hydroxides; this assumption is justified by the positive correlation between FeO and Al$_2$O$_3$ observed in the investigated samples (Supplementary Fig. S3b), which suggests that FeO was mostly sequestered within Al$_2$O$_3$-rich phyllosilicates, and by the negative correlation between FeO and CaO (Supplementary Fig. S3c), which implies that the ankerite component was negligible in the protoliths. (3) Illite and K-feldspar, rather than (detrital) muscovite, are the only K$_2$O-bearing phases in the protolith. (4) Sulphur-bearing phases (sulphides and sulphates) can be neglected. In fact, if the protoliths would have contained sulphur-bearing phases in significant amounts, their metamorphic products should also contain abundant sulphur-bearing minerals, which is not the case for the studied samples. Finally, the possible occurrence of organic carbon in the original sediments does not influence the estimate of the protolith mineral assemblages, and especially its initial carbonates amount. In fact, carbon is not considered as an independent component in the least-square calculations, and the initial amount of carbonates is constrained based on the amounts of CaO and MgO only. The results obtained for each sample are presented in the Dataset 3 in the Supplementary Material, whereas Table 1 summarises the results for the eight samples investigated in detail in this study.

Forward thermodynamic modelling

The forward thermodynamic modelling approach was applied to seven of the eight samples investigated in this study. The P/T-X(CO$_2$) mineral assemblage diagrams were calculated using

Perple_X (Connolly, 1990, 2009), version 6.9.1, the internally consistent thermodynamic dataset from Holland & Powell (1998, update 2004) (ds55) and the EoS of Holland & Powell (1998) for binary H$_2$O–CO$_2$ molecular fluids and assuming fluid saturation conditions. The following solution models have been used: carbonate (i.e. Ca–Mg–Mn–Fe carbonate with calcite structure; Massonne, 2010), garnet, chloritoid, staurolite, cordierite, epidote, dolomite and clinopyroxene (Holland & Powell, 1998), biotite (White *et al.*, 2007), chlorite (Holland *et al.*, 1998), feldspar (Fuhrman & Lindsley, 1988), white mica (Coggon & Holland, 2002; Auzanneau *et al.*, 2010), ilmenite (White *et al.*, 2014), clino- and ortho-amphibole (Diener *et al.*, 2007; Diener & Powell, 2012), talc (ideal model) and scapolite (Kuhn *et al.*, 2005). Quartz, titanite, zoisite, kyanite/sillimanite and rutile were considered as pure phases. The P/T gradient was defined based on the P–T evolution constrained from the associated metapelites (Tamang *et al.*, 2023), i.e. a prograde stage characterised by an increase in both P and T conditions up to peak P conditions, and a decompression stage from peak P to peak T conditions. The P/T gradient for the prograde stage was defined as $P(\text{bar}) = 17T\ (K) - 5065$, in the temperature interval 400–600 °C; the P/T gradient for the decompression stage was defined as $P(\text{bar}) = -63.8T\ (K) + 65\,473$, in the temperature interval 600–700 °C. Each P/T-X(CO$_2$) pseudosection thus consists of two parts, with the junction located at 600 °C, 9.8 kbar. The P/T-X(CO$_2$) pseudosections were calculated in the full MnO–Na$_2$O–K$_2$O–CaO–FeO–MgO–Al$_2$O$_3$–SiO$_2$–TiO$_2$–Fe$_2$O$_3$–H$_2$O–CO$_2$ (MnNKCFMASTO–H$_2$O–CO$_2$) system (sample 17b-12) or in the reduced NKCFMASTO–H$_2$O–CO$_2$ (sample 17b-36b), MnNKCFMAST–H$_2$O–CO$_2$ (samples 17a-29 and 17a-35), NKCFMAST–H$_2$O–CO$_2$ (samples 15a-28a and 18a-26) and CFMAS-HC (sample 17b-7d) systems, according to the observed mineral assemblages and compositions (e.g. MnO was included to model the garnet-bearing samples; Fe$_2$O$_3$ was included to model samples containing white mica anomalously enriched in Fe^{3+}). Fractionation effects on the bulk composition due to the growth of garnet porphyroblasts in samples 17b-12, 17a-29 and 17a-35 were not considered; however, the garnets are relatively poorly zoned or even compositionally homogeneous (sample 17b-12). Although we recognise the overall simplifications of the model setups described above (e.g. we did not consider more complex fluids beyond the H$_2$O–CO$_2$ binary, nor the fractionation effects on the bulk compositions due to the growth of garnet porphyroblasts), these are inevitably required by the complexity of the modelling. Minor discrepancies between the observed and modelled mineral assemblages and compositions (see below) may in any case be related to this simplified approach.

The P–T–X(CO$_2$) evolution of the modelled samples was constrained using the following strategy: (1) the initial P–T–X(CO$_2$) conditions were set at T = 400 °C (P = 6.4 kbar) and at an X(CO$_2$) value such that the predicted mineral modes are as close as possible to the calculated mineral modes of the protolith (with muscovite replacing illite ± K-feldspar, Al-rich minerals such as pyrophyllite or chloritoid replacing kaolinite, and paragonite replacing albite); (2) prograde conditions were inferred from the intersection of compositional isopleths (XMn, XMg and XCa) modelled for the garnet core in those samples where garnet porphyroblasts are slightly zoned (samples 17a-29 and 17a-35); (3) peak conditions were inferred from the intersection of compositional isopleths modelled for biotite ± plagioclase ± hornblende ± ortho-amphibole ± garnet rim, depending on the observed peak assemblages. XMg isopleths were used for biotite, hornblende, and ortho-amphibole, XCa isopleths for plagioclase and XMn, XMg and XCa isopleths for garnet rim. Systematically, two isopleths were

used for each compositional parameter, corresponding to the measured compositional range in each phase; where the modelled compositional isopleths are mostly parallel to each other, allowing good estimates of peak P–T conditions but poor definition of the fluid composition, the peak $X(CO_2)$ values are further constrained according to the best fit between observed and modelled mineral modes. The only exception is sample 17b-7d (magnesite + talc rock), for which compositional isopleths have not been used due to the almost pure composition of all phases (approaching the Mg end-members) and the peak conditions were thus inferred directly from the intersection of the modelled isomodes for magnesite, talc and chlorite.

Estimate of the amount of CO_2 produced

The amount (wt%) of CO_2 released from each sample was estimated from the amount of carbonates consumed along the inferred P–T–$X(CO_2)$ evolution, calculated as the difference between the carbonates originally present in the protolith and those still preserved at peak conditions. The following reasoning is used to convert carbonate modal amounts (vol%) to CO_2 amounts (wt%): 1 vol% of dolomite/magnesite corresponds to 1 cm³ of dolomite/magnesite in 100 cm³ of rock; dolomite and magnesite have densities of 2.86 and 2.98 g/cm³ (Deer *et al.,* 1992), respectively, whereas an average density of 2.7 g/cm³ is assumed for the host rock. This means that 1 vol% dolomite/-magnesite corresponds to 2.86 g/270 g = 1.06 wt% dolomite and 2.98 g/270 g = 1.10 wt% magnesite. One mole of dolomite $(CaMg(CO_3)_2)$ weighs 184 g $(CaO + MgO + 2CO_2 = 56 + 40.3 + 2 \times 44$ g/mol) and 1 mol of magnesite $(MgCO_3)$ weighs 84 g $(MgO + CO_2 = 40.3 + 44$ g/mol). This means that 1 g of dolomite contains 0.48 g of CO_2, and 1 g of magnesite contains 0.52 g of CO_2. To obtain the amount of CO_2 released by 1 vol% of dolomite, we must therefore multiply 1.06 wt% × 0.48 = 0.51 wt% of CO_2, and for magnesite, we must multiply 1.10 wt% × 0.52 = 0.57 wt% of CO_2.

The wt% CO_2 punctual data obtained from the studied dolomitic and magnesitic samples were tentatively fitted using a non-linear rational equation of this type: $y = (a + cx + ex^2 + gx^3 + ix^4 + kx^5)/(1 + bx + dx^2 + fx^3 + hx^4 + jx^5)$, where y is the wt% CO_2, x is the original carbonate amount (vol%) in the protolith and the a to k coefficients are provided in Table S3 of the Supplementary Material. The fitting equations, calculated using TableCurve_2D (Systat Software), allow defining average curves that represent the best fit of the punctual data; the minimum and maximum curves enveloping the punctual data provide the error values associated to the estimate of the amount of CO_2 produced. The same approach was applied to 11 samples belonging to the calcite series, already investigated by Groppo *et al.* (2017, 2021, 2022) and Rapa *et al.* (2017). Due to the limited number of data, this fitting procedure should be considered as approximate.

RESULTS
Protolith assemblages

Processing of the bulk-rock chemical analyses using the method described above allowed the approximate protolith assemblages to be reconstructed for all samples. It appears that most of the LHS lithologies are derived from the metamorphic transformation of dolomitic and magnesitic protoliths in which calcite was virtually absent, with only a few samples derived from calcite-bearing sediments. This contrasts with the data from the GHS lithologies, which are entirely derived from calcite-bearing protoliths, suggesting different depositional environments for the

LHS and GHS (Table S1 in the Supplementary Material). The bulk chemical data, plotted on the CaO–Al₂O₃–MgO diagram (Fig. 2), define three distinct linear trends linking the calcite, dolomite and magnesite compositions to the average pelite field. Based on the type of carbonate mineral originally dominant in the protolith, the samples were therefore classified into three groups: (i) a calcite series, (ii) a dolomite series and (iii) a magnesite series. Each series includes rocks derived from protoliths that originally contained varying amounts of carbonates, ranging from less than 10% to more than 80% (% expressed by volume throughout the text), and are classified as calcareous pelites (calcite <15%), marls *sensu stricto* (calcite 15–50%) and limestones (calcite >50%) for the calcite series; dolomitic pelites (dolomite <15%), dolomitic marls (dolomite 15–50%) and dolostones (dolomite >50%) for the dolomite series; magnesitic pelites (magnesite <15 vol%), magnesitic marls (magnesite 15–50%) and magnesite ores (magnesite >50%) for the magnesite series (Fig. 2 and Table S1 in the Supplementary Material). Irrespective of the original amount of carbonate minerals, most of the protoliths reflect moderate degrees of weathering (i.e. K-feldspar is still preserved); higher degrees of weathering are suggested for a few of them (e.g. samples 17a-29 and 17a-35 from the Benighat Slates Formation), which contain kaolinite rather than K-feldspar (Fig. S2a in the Supplementary Material). The silicate fraction of the analysed protoliths consists of clay minerals, quartz and feldspar in variable proportions and generally reflects a moderate degree of maturity (Fig. S2b in the Supplementary Material), except for some dolostones and magnesitic rocks, in which the scarce silicate fraction is dominated by quartz.

Metamorphic assemblages and mineral compositions

Eight samples were considered for the petrographic and microstructural analysis, five from the dolomite series and three from the magnesite series. An overview of the samples at the thin section scale is given in Fig. 3, while representative microstructures are shown in Figs 4–7. Assemblages and modal compositions of all samples are given in Table 2. Mineral chemical results are summarised in Fig. S8 and discussed in detail in the Supplemental Material, while only the compositional parameters used to interpret the phase diagram modelling results are reported here.

Dolomite series

Sample 17b-12. In this two-mica, plagioclase + garnet-bearing schist, the main foliation (S_m) is defined by muscovite and biotite, which are concentrated in multi-mm continuous layers alternating with mm-thick quartz layers (Fig. 4a). The brown-red biotite (XMg = 0.53–0.57) occurs in two different generations: fine-grained flakes, syn-kinematic with respect to the S_m and coarse-grained flakes, statically and discordantly overgrowing the S_m (Fig. 4a). Plagioclase is strongly zoned, with a Na-rich core (XCa = 0.28–0.49) and a Ca-rich rim (XCa = 0.60–0.71), and is post-kinematic with respect to S_m (Fig. 4c). The multi-mm-sized garnet porphyroblasts ($Alm_{65-67}Grs_{19-21}Prp_{10-11}Sps_{3-4}$) have a skeletal habit and overgrow the S_m (Figs 3a and 4b). The fine-grained epidote is zoned, with allanitic core and clinozoisite rim.

Sample 17a-29. This is a garnet + plagioclase + kyanite + staurolite-bearing biotitic schist. The main foliation (S_m) is defined by biotite forming mm-thick discontinuous layers alternating with mm-thick quartzitic layers (Fig. 4d); the schistosity is partially obscured by static overgrowth of abundant plagioclase (Fig. 4e, g). Biotite (XMg = 0.67–0.71) occurs in two distinct generations: a syn-S_m generation, oriented to define the main foliation,

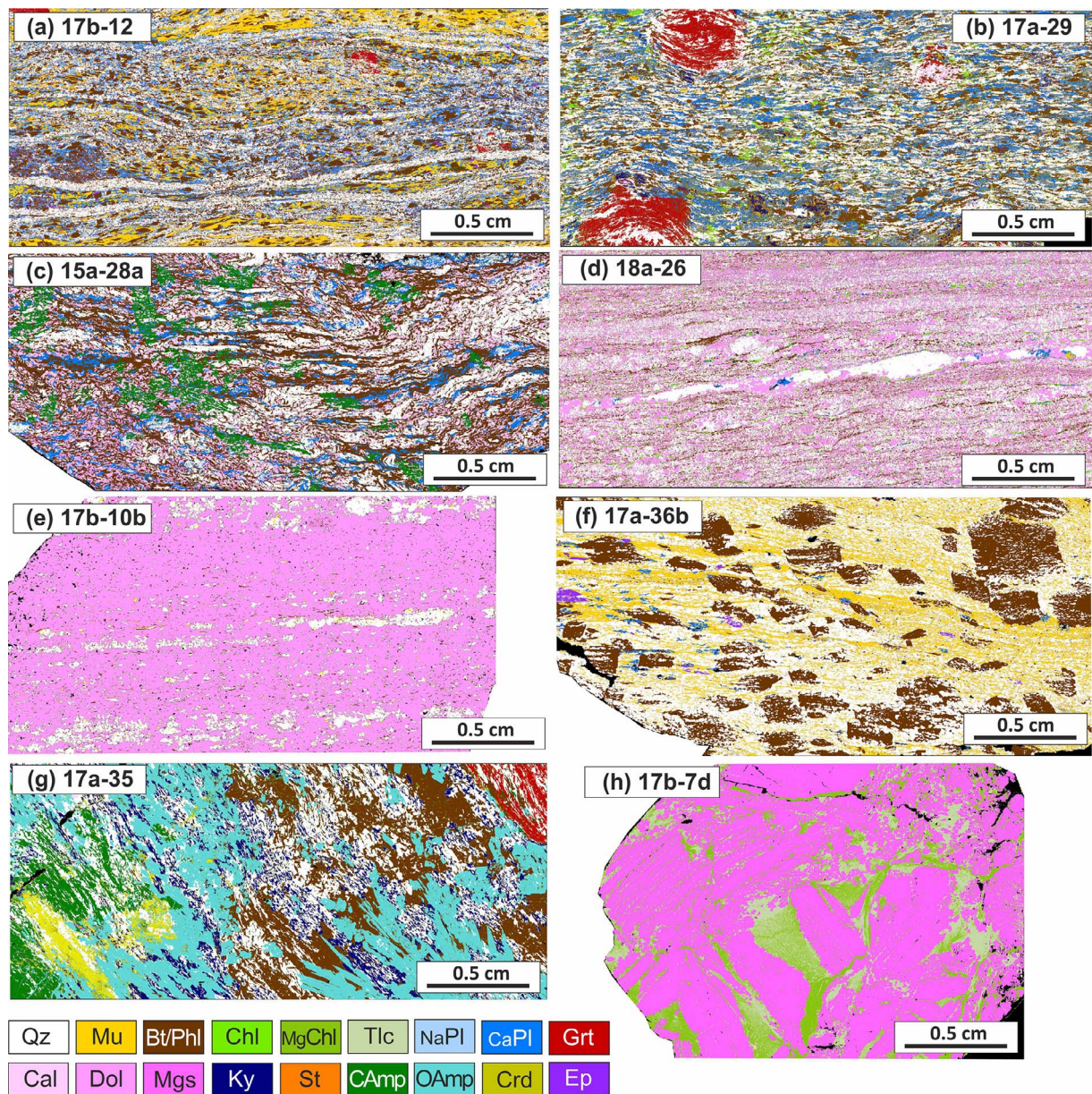| Qz | Mu | Bt/Phl | Chl | MgChl | Tlc | NaPl | CaPl | Grt |
| Cal | Dol | Mgs | Ky | St | CAmp | OAmp | Crd | Ep |

Fig. 3. Processed X-ray maps of the studied carbonate-bearing lithologies from the dolomite series (a: 17b-12; b: 17a-29; c: 15a-28a; d: 18a-26; e: 17b-10b) and the magnesite series (f: 17a-36b; g: 17a-35; h: 17b-7d). For sample 17a-36b, note that although not present in the thin section used for the SEM-EDS map, kyanite was additionally observed in another thin section from the same sample (see Fig. 6b).

and a post-S_m generation, occurring as large flakes overgrowing S_m discordantly. The multi-mm garnet porphyroblasts (core: $Alm_{58-59}Grs_{20-22}Prp_{10-12}Sps_{8-11}$; rim: $Alm_{58-61}Grs_{18-20}Prp_{15-17}Sps_{5-6}$) are syn- to post-kinematic with respect to S_m and systematically occur in the carbonate-rich microstructural domains (Fig. 3b; see also Fig. S4a in the Supplementary Material). They contain an internal foliation defined by quartz, carbonate (Fig. 4f) and graphite inclusions, which is continuous with the external S_m but more widely spaced (Fig. 4d). Plagioclase ($XCa = 0.72–0.84$; few cores: $XCa = 0.55–0.61$) forms mm-sized porphyroblasts that overgrow S_m (Fig. 4e) and include corroded carbonate relics (Fig. 4g). The mm-sized kyanite and staurolite porphyroblasts are post-kinematic with respect to S_m (Fig. 4e). Plagioclase, kyanite and staurolite are replaced by fine-grained muscovite at the rim (Fig. 4g). Carbonates (dolomite and calcite) are finely dispersed in the matrix and locally form multi-mm aggregates together with

quartz (Fig. 3b). The occurrence of (i) skeletal garnet adjacent to these carbonate-rich aggregates (Fig. S4a in the Supplementary Material), (ii) abundant carbonate inclusions within large garnet porphyroblasts (Fig. 4f and Fig. S4b–d in the Supplementary Material) and (iii) relict corroded carbonates within plagioclase porphyroblasts (Fig. 4g) suggests that carbonates are involved in the garnet- and plagioclase-forming reaction(s). Among the carbonates in the matrix, dolomite occurs systematically as rounded inclusions within calcite, suggesting that calcite could be, at least in part, a late phase. Chlorite is a retrograde mineral, mostly developed at the expense of biotite.

Sample 15a-28a. In this amphibole-bearing phlogopite calc-schist, the main foliation (S_m) is marked by pale brown phlogopite ($XMg = 0.81–0.83$), which defines mm-thick continuous layers alternating with multi-mm-thick quartzitic layers (Fig. 5a). S_m is crenulated, with the development of asymmetric open folds
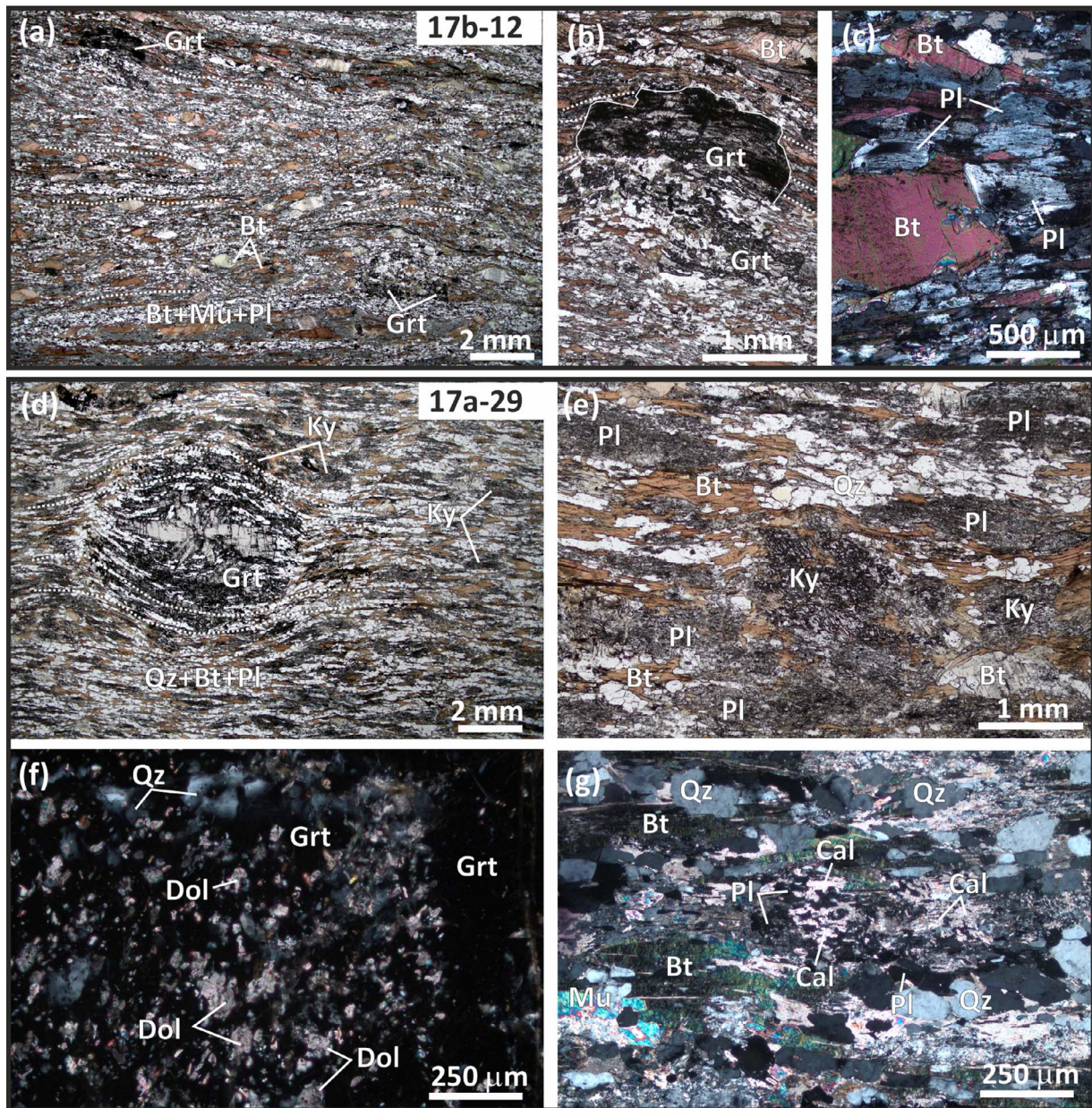
Fig. 4. Representative assemblages and microstructures of samples from the dolomite series 17b-12 (a-c) and 17a-29 (d-g). White dotted lines in all the photographs represent the main foliation S_m. Sample 17b-12: (a) the main foliation defined by fine-grained muscovite and biotite, overgrown by biotite porphyroblasts (plane polarised light: PPL); (b) skeletal garnet porphyroblast overgrowing S_m (PPL); (c) post-kinematic plagioclase and biotite overgrowing S_m (crossed polarised light, XPL). Sample 17a-29: (d) multi-mm garnet porphyroblast including an internal foliation continuous with S_m, but more widely spaced (PPL); (e) kyanite and plagioclase overgrowing S_m (PPL); (f) fine-grained relict dolomite inclusions within a garnet porphyroblast (XPL); (g) corroded carbonate inclusions within plagioclase porphyroblasts (XPL).

(Fig. 3c); an axial planar foliation (S_{m+1}) occurs locally, defined by phlogopite. Carbonate minerals (calcite and dolomite) are abundant and distributed in the main foliation, where they show equilibrium relationships with phlogopite (Figs 3c and 5a and Fig. S5d–f in the Supplementary Material). The occurrence of rounded inclusions of dolomite within calcite (Fig. S5c in the Supplementary Material) suggests that at least some calcite developed at the expense of dolomite. Plagioclase (XCa = 0.76–0.90) forms mm-sized porphyroblasts overgrowing both S_m and S_{m+1} (Fig. 3c). Colourless amphibole (magnesio-hornblende: XMg = 0.85–0.90) forms multi-mm-sized porphyroblasts statically overgrowing both S_m and crenulation folds (Figs 3c and 5a). Amphibole porphyroblasts are poikiloblastic with rounded/corroded inclusions of quartz, dolomite, calcite and plagioclase

(Fig. 5b and Fig. S5a–c in the Supplementary Material), indicating that all these phases were reactants of the amphibole-forming reaction(s).

Sample 18a-26. This sample is a phlogopite + kyanite-bearing dolomitic calcschist. The main foliation (S_m) is defined by phlogopite concentrated in thin and discontinuous layers alternating with multi-mm-thick layers dominated by dolomite and quartz (Figs 3d and 5c). A mm-thick vein occurs parallel to the main foliation and is mostly filled by quartz and dolomite, which are coarser grained than the matrix (Fig. 3d). Phlogopite (XMg = 0.94–0.95) shows weak pleochroism ranging from very pale brown to colourless. Most of the dolomite is fine grained and dispersed in the matrix; dolomite also forms multi-mm fine-grained aggregates enveloped by the main foliation, locally
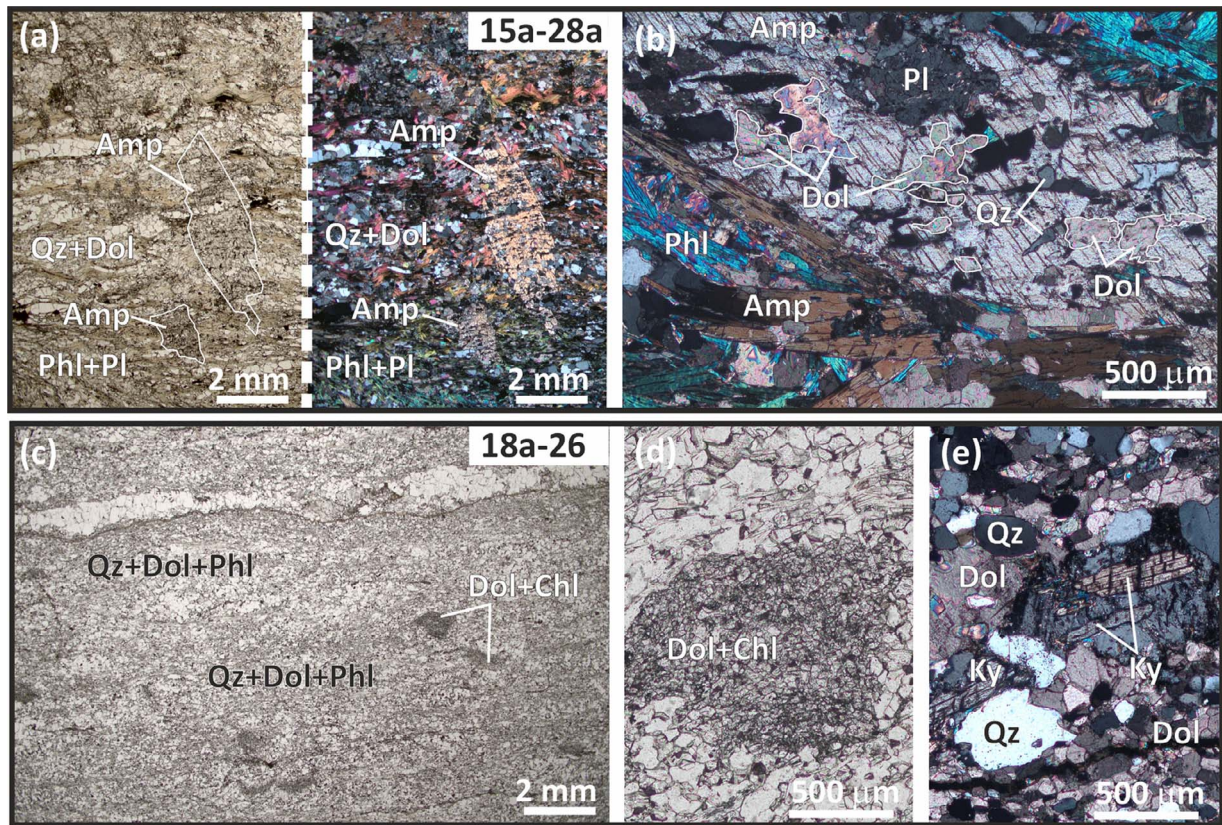
Fig. 5. Representative assemblages and microstructures of samples from the dolomite series 15a-28a (a-b) and 18a-26 (c-e). Sample 15a-28a: (a) the main foliation S_m defined by phlogopite, overgrown by hornblende porphyroblasts (PPL/XPL); (b) corroded inclusions of dolomite, quartz and plagioclase within a hornblende porphyroblast (XPL). Sample 18a-26: (c) the main foliation S_m defined by fine-grained phlogopite; note the quartz-rich vein parallel to the S_m at the top; (d) fine-grained aggregate of dolomite with chlorite inclusions, enveloped by the main foliation (PPL); (e) detail of small grains of kyanite, aligned with S_m (XPL).

including minor chlorite flakes (Fig. 5d). Dolomite appears homogeneous under CL, with a dark red luminescent colour (Supplementary Fig. S7a). Plagioclase is mostly concentrated within the quartz-rich vein ($XCa = 0.12$–0.28) but also occurs as randomly dispersed blasts in the matrix ($XCa = 0.45$–0.48 to $XCa = 0.56$–0.69). The sub-mm kyanite is concentrated in thin layers parallel to S_m (Fig. 5e), which is particularly evident under CL due to its bright luminescence (Supplementary Fig. S7a). Late muscovite replaces plagioclase. Chlorite is also mostly a retrograde mineral, developed at the expense of phlogopite, except for a few flakes included in the fine-grained aggregates of dolomite, which are interpreted as prograde relics.

Sample 17b-10b. This is an impure phlogopite-bearing dolomitic marble with a banded structure defined by mm- to multi-mm-thick silicate-rich layers alternating with cm-thick carbonatic layers (Fig. 3e). The dolomite is granoblastic and fine grained, except for a few coarse-grained blasts concentrated in the silicate-rich layers. Under CL, the dolomite mostly shows a homogeneous dark red luminescence, with a few exceptions: (i) some fine-grained interstitial grains appear bright yellow and zoned (Supplementary Fig. S7b), and (ii) the coarse-grained blasts in the silicate-rich layers are slightly zoned, with very dark red cores and dark red rims (Supplementary Fig. S7b). The main foliation (S_m) is defined by very pale brown phlogopite ($XMg = 0.96$–0.97) and minor muscovite. The latter also occurs as a late phase locally replacing K-feldspar. A small amount of fine-grained K-feldspar ($XOr = 0.93$–0.95) is randomly distributed within the dolomite matrix.

Magnesite series

Sample 17a-36b. This sample is a muscovite schist with phlogopite, plagioclase and epidote ± kyanite porphyroblasts. The main foliation (S_m) is marked by muscovite and minor phlogopite, which define thin layers interbedded with quartz-rich layers (Fig. 6a). Phlogopite, plagioclase, epidote and kyanite porphyroblasts statically overgrow S_m (Fig. 3f and 6a–c). Phlogopite ($XMg = 0.91$–0.93) forms multi-mm post-S_m porphyroblasts, but it also occurs as finer-grained flakes aligned with S_m (Fig. 6a). Plagioclase porphyroblasts ($XCa = 0.32$–0.37) are mm sized and have a skeletal habit (Fig. 6c), and epidote is strongly zoned, with allanitic core and clinozoisite rim.

Sample 17a-35. This is an amphibole + kyanite + garnet + cordierite-bearing phlogopite schist. The sample has a banded structure (Fig. 3g) with alternate multi-cm domains that are either phlogopite rich (phlogopite + kyanite + orthoamphibole + garnet) or amphibole rich (Ca-amphibole + orthoamphibole + cordierite + minor Mg-chlorite). The main foliation (S_m) is defined by pale brown phlogopite ($XMg = 0.79$–0.82) in the phlogopite-rich domains and by orthoamphibole (anthophyllite: $XMg = 0.67$–0.73) and minor Mg-chlorite in the amphibole-rich domains (Fig. 6d, e, h). S_m is almost completely obscured by the static overgrowth of multi-mm to cm-sized porphyroblasts of orthoamphibole, garnet, kyanite, Ca-amphibole and/or cordierite (Fig. 3g). In the phlogopite-rich domains, the porphyroblasts overgrowing S_m are (i) cm-sized garnet (GrtC: $Alm_{62-65}Grs_{14-16}Prp_{20-23}Sps_1$; GrtR: $Alm_{57-62}Grs_{10-14}Prp_{25-32}Sps_{0-0.5}$), including an internal foliation defined by quartz, continuous with S_m (Figs 3g and 6e), and (ii)
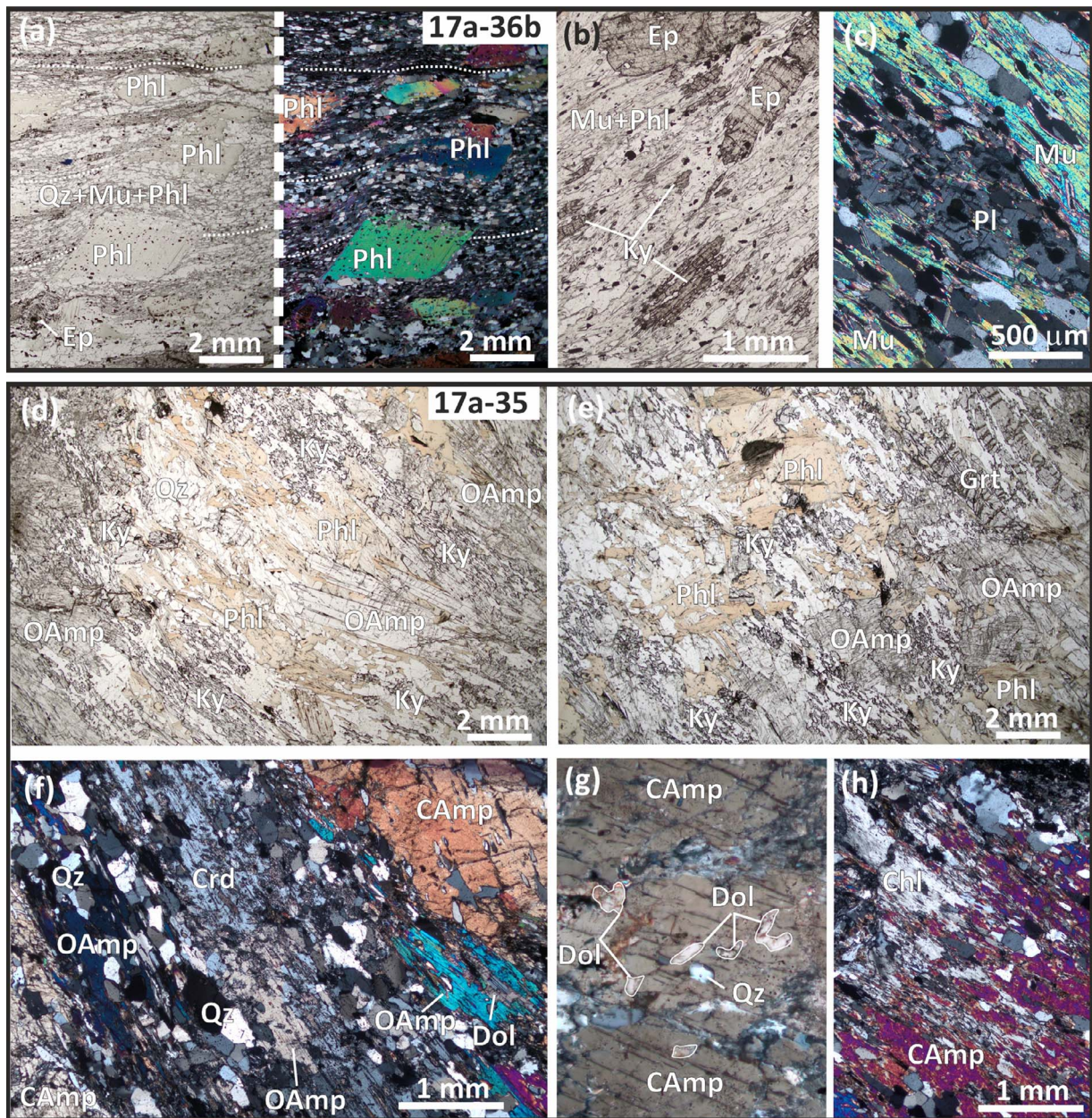
Fig. 6. Representative assemblages and microstructures of samples from the magnesite series 17a-36b (a–c) and 17a-35 (d–h). Sample 17a-36b: (a) phlogopite porphyroblasts overgrowing S_m defined by muscovite and minor fine-grained phlogopite (PPL/XPL); (b) epidote and kyanite porphyroblasts overgrowing S_m (PPL); (c) plagioclase overgrowing S_m (XPL). Sample 17a-35: (d, e) post-kinematic ortho-amphibole (d, e), kyanite (d, e) and garnet (e) overgrowing S_m (PPL); (f) post-kinematic cordierite, Ca-amphibole, and ortho-amphibole overgrowing S_m; note the relict dolomite included within ortho-amphibole, overgrowing Ca-amphibole (XPL); (g) relict dolomite inclusions within Ca-amphibole (XPL); (h) relict Mg-chlorite overgrown by Ca-amphibole (XPL).

multi-mm skeletal kyanite, partially intergrown with (iii) multi-mm colourless orthoamphibole (Figs 6d, e). In the amphibole-rich domains, the porphyroblastic phases are (i) multi-mm green Ca-amphibole (aluminous-tschermackite: $XMg = 0.80$–0.85), locally overgrowing relict Mg-chlorite and partially replaced by orthoamphibole (Figs 6f–h), and (ii) multi-mm cordierite ($XMg = 0.52$–0.83), elongated along and overgrowing S_m (Fig. 6f). The occurrence of very rare carbonate relics within the porphyroblastic Ca-amphibole (Fig. 6g) and in the orthoamphibole overgrowing it (Fig. 6f) suggests that carbonates are involved in the Ca-amphibole forming reaction(s).

Sample 17b-7d. This sample is a magnesite + talc + chlorite rock (Fig. 3h). The magnesite is medium to coarse grained and

highly heterogeneous in grain size (Fig. 7a). Most of the magnesite crystals are multi-mm to cm sized and often have an elongated habit. The coarse-grained magnesite crystals have a cloudy appearance because they are crowded with fluid and solid inclusions, while the thin rims in contact with the surrounding talc ± chlorite are clear (Fig. 7a). The very fine-grained solid inclusions are particularly abundant in the cores of the multi-cm-sized magnesite and consist mostly of rounded inclusions of dolomite and apatite. The microstructural zoning observed in the coarse-grained magnesite crystals is also evident under CL, with the large magnesite cores showing a red luminescence that contrasts with the very dark red luminescence colour of the rims (Fig. 7b; Supplementary Fig. S7c). The coarse-grained
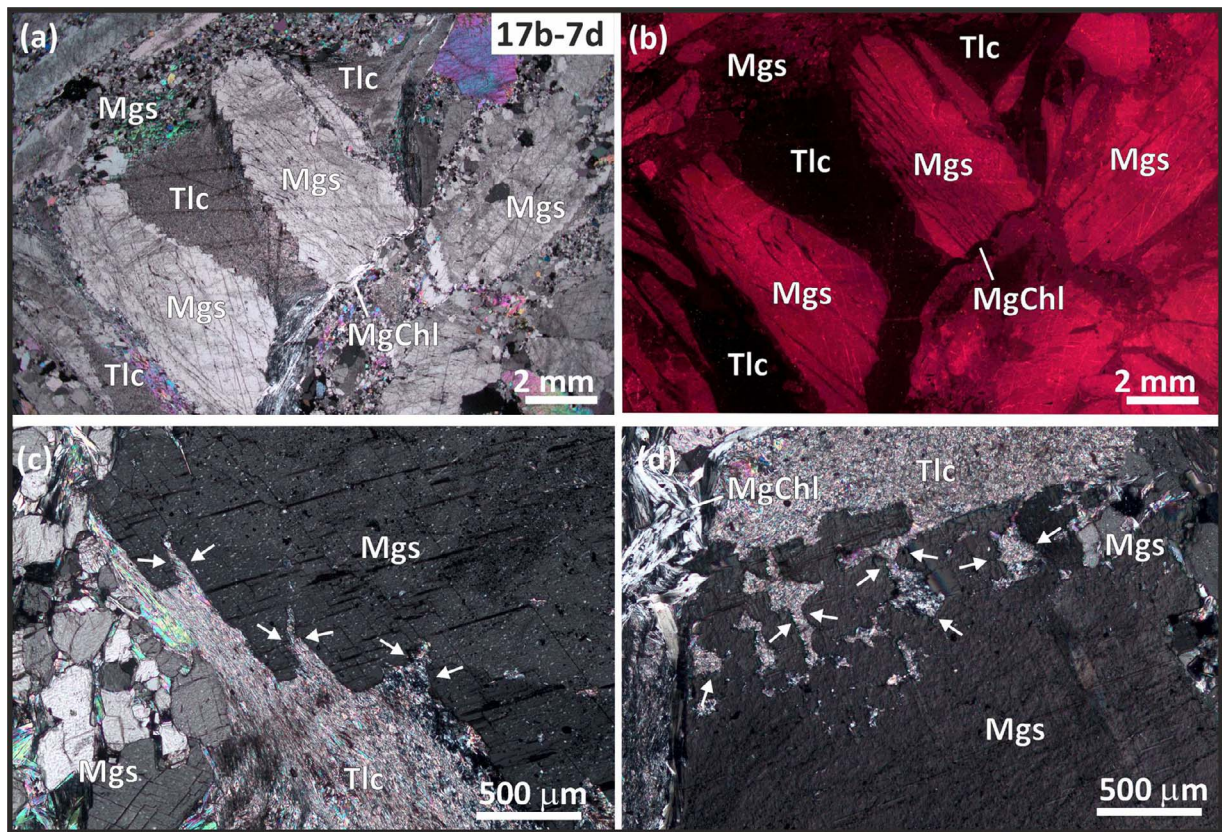
Fig. 7. Representative assemblages and microstructures of sample 17b-7d from the magnesite series. (a) Coarse-grained magnesite partially replaced by the second generation of magnesite associated with talc and Mg-chlorite (XPL). (b) CL image showing the large luminescent cores of the coarse-grained magnesite surrounded by a thin rim of dark luminescence. (c, d) Details of the fine-grained talc and Mg-chlorite replacing magnesite at the rim (XPL).

magnesite is replaced at the rim and along fractures by very fine- to medium-grained talc (XMg = 0.98–1.00) and fine-grained Mg-chlorite (XMg = 0.98–1.00) (Fig. 7c, d) associated with a second generation of fine-grained magnesite, granoblastic and with a clear appearance. This second generation of magnesite shows the same very dark red luminescence colours as the rims of the coarse-grained magnesite (Fig. 7b).

Thermodynamic modelling

The thermodynamic modelling approach was applied to seven samples (two dolomitic pelites: 17b-12, 17a-29; two dolomitic marls: 15a-28a, 18a-26; one magnesic pelite: 17a-36b; one magnesitic marl: 17a-35; and one magnesite ore: 17b-7d) to constrain their $P–T–X(CO_2)$ evolution and decarbonation history. Sample 17b-10b (dolomitic marble) was not modelled because the comparison between the calculated amounts of dolomite in the protolith and the observed amounts of dolomite in the sample suggests that dolomite was not consumed during metamorphism (i.e. decarbonation reactions did not occur; see the Discussion section for further explanations). The $P/T-X(CO_2)$ mineral assemblage diagrams were calculated along a P/T gradient defined on the basis of the P–T evolution constrained from the associated metapelites (see above). In interpreting the phase diagrams, it is therefore important to note that while the temperature increases regularly along the vertical axis, the pressure increases up to 600 °C and then decreases at T > 600 °C. The main topological features of the calculated phase diagrams are described in detail in the Supplementary Material; this section summarises the modelling results that allow constraints to be placed on the

initial, prograde and peak conditions. The compositional isopleths modelled for each sample and used to constrain the prograde and peak $P–T–X(CO_2)$ conditions are shown in Supplementary Fig. S9, while a comparison between the observed and modelled modal compositions for each sample is shown in Figs 8–14. It is worth noting that, despite the complexity of the modelling, the results are consistent with the mineral assemblages and modes observed in all samples, even in the case of relatively uncommon assemblages; there is also a generally good agreement between modelled and measured mineral compositions for all samples. This good agreement between models and observations confirms the reliability of the $P–T–X(CO_2)$ estimates obtained.

Dolomite series

For all the samples belonging to the dolomite series, the starting point for the $P–T–X(CO_2)$ evolution is fixed at 400 °C, $X(CO_2) = 0.02$, following the strategy discussed above. Prograde and peak conditions for each sample are defined as follows:

Sample 17b-12. The compositional isopleths modelled for garnet (XMg = 0.10–0.11, XCa = 0.19–0.21, XMn = 0.03–0.04) converge in the very narrow field Qz + Mu + Pg + Bt + Chl + Ep + Mgs + Grt + Ilm, constraining garnet nucleation at T = 560–580 °C, P = 9.1–9.4 kbar, $X(CO_2) \approx 0.2$ (Fig. 8a and Supplementary Fig. S9a), and suggesting that the appearance of garnet is related to the breakdown of carbonate minerals, even if carbonates are no longer preserved in the sample likely because of the very low amount of carbonates involved (see below). The observed peak assemblage (Qz + Mu + Bt + Grt + Pl + Ep) is modelled by a large field at T = 600–620 °C, extended over the entire $X(CO_2)$ interval (Fig. 8a).

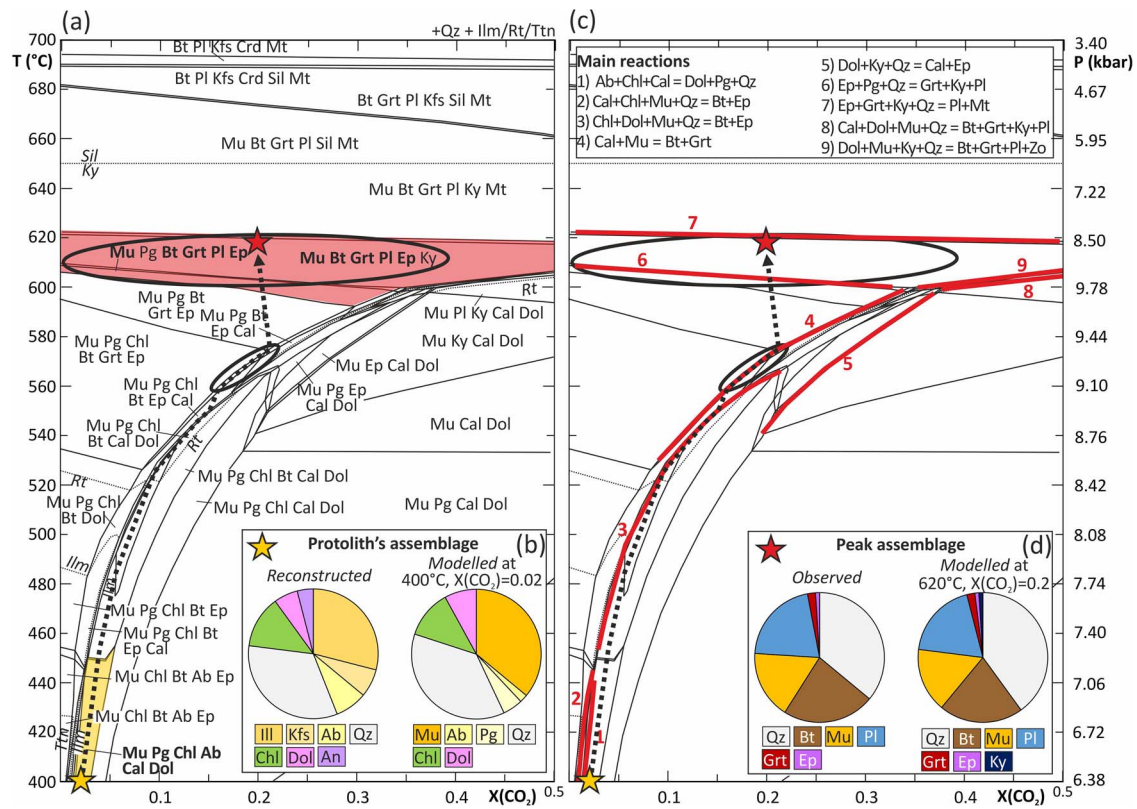**Fig. 8.** (a) P/T-X(CO_2) mineral assemblage diagram modelled for sample 17b-12. The variance of the fields varies from two (i.e. ten phases) to seven (i.e. five phases). Dotted lines delineate the stability fields of the Ti-bearing accessory minerals (titanite, rutile, ilmenite). The yellow field is the modelled stability field of the protolith assemblage; the red fields correspond to the stability fields of the peak assemblage (for each modelled assemblage, the observed minerals are shown in bold). Yellow and red stars refer to the 'starting point' and peak conditions, respectively, as discussed in the text. The black ellipses summarise the prograde and peak conditions. (b) Comparison between the reconstructed protolith assemblage and that modelled at the 'starting point'. (c) Same plot as (a), highlighting the isothermal/isobaric univariant equilibria relevant to this sample. Note that the univariant curves overlap the narrow low-variant fields of the pseudosection. Reactions are written so that the products are on the high-T side of the equilibrium curves. (d) Comparison between the observed peak assemblage and that modelled at peak conditions. The black ellipses and dotted black arrows in (a) and (c) summarise the prograde and peak conditions and approximate the P–T–X(CO_2) evolution inferred for sample 17b-12 as discussed in the text.

Kyanite is modelled in this field, but it is not observed in the sample. However, this is a minor discrepancy as the predicted amount of kyanite is very low (<1.5%; Fig. 8d). Garnet is mostly unzoned in this sample; this is consistent with the modelled compositional isopleths, which do not predict significant changes in garnet composition from the prograde to the peak stage (Supplementary Fig. S9a). The modelled XMg and XCa isopleths for biotite and plagioclase in the peak assemblage field agree well with the measured compositions (biotite: XMg = 0.53–0.57; plagioclase core: XCa = 0.28–0.49; plagioclase rim: XCa = 0.60–0.71) (Supplementary Fig. S9a). The modelled mineral modes converge to the observed ones at 620 °C, X(CO_2) = 0.2 (Fig. 8d), which are therefore inferred to be the peak T-X(CO_2) conditions.

Sample 17a-29. The modelled compositional isopleths for the garnet core (GrtC: XMg = 0.10–0.12, XCa = 0.20–0.22, XMn = 0.08–0.11) constrain its growth during the prograde stage at T = 550–570 °C, P = 8.8–9.2 kbar (in the Mu + Chl + Grt + Ky + Cal + Dol field) (Fig. 9a and Supplementary Fig. S9b). The observed peak assemblage (Qz + Bt + GrtR + Ky + Pl + St + Dol, ±Mu ± Cal) is modelled by a series of narrow fields located at T = 600–615 °C, P = 8.8–9.8 kbar, X(CO_2) > 0.3 (Fig. 9a). Indeed, calcite and dolomite are predicted to be stable at T < 610 °C and T < 615 °C, respectively, whereas biotite and plagioclase only appear at T > 600 °C for X(CO_2) > 0.3. This suggests that most of the minerals in this sample grew during the decompression stage. Further constraints on the peak T-X(CO_2) conditions are provided by the

modelled compositional isopleths of the post-kinematic garnet rim (GrtR: XMg = 0.15–0.17, XCa = 0.18–0.20, XMn = 0.05–0.06), combined with those of biotite (XMg = 0.68–0.71) and plagioclase (XCa = 0.72–0.84, and few cores analysis with XCa = 0.55–0.61), all converging at P–T–X(CO_2) conditions of 610 °C, X(CO_2) = 0.5 (Supplementary Fig. S9b). Staurolite, which occurs in low modal amounts at the same microstructural position as kyanite (i.e. post-kinematic phase), is not predicted at the inferred peak conditions (Fig. 9d). This minor discrepancy could be related to the simplification of not considering the possible effects of chemical fractionation on the bulk composition due to the growth of garnet. In fact, the modelled mineral modes are in good agreement with the observed ones (Fig. 9d).

Sample 15a-28a. The observed peak assemblage (Qz + Bt + Hbl + Pl + Dol + Cal) is modelled by a field located at T = 610–620 °C, P = 8.5–9.1 kbar, X(CO_2) > 0.45 (Fig. 10a); dolomite is modelled as the only carbonate mineral at these conditions, but the predicted modal amount of dolomite (22%) is close to the observed amount of dolomite + calcite (21%) (Fig. 10d). The XMg and XCa isopleths modelled for biotite/hornblende and plagioclase, respectively, and corresponding to their measured compositions (biotite: XMg = 0.81–0.83; hornblende: XMg = 0.85–0.90; plagioclase: XCa = 0.76–0.90), converge at the inferred peak conditions of 620 °C, X(CO_2) = 0.5 (Supplementary Fig. S9c); at these conditions, there is also a relatively good agreement between observed and modelled mineral modes (Fig. 10d).
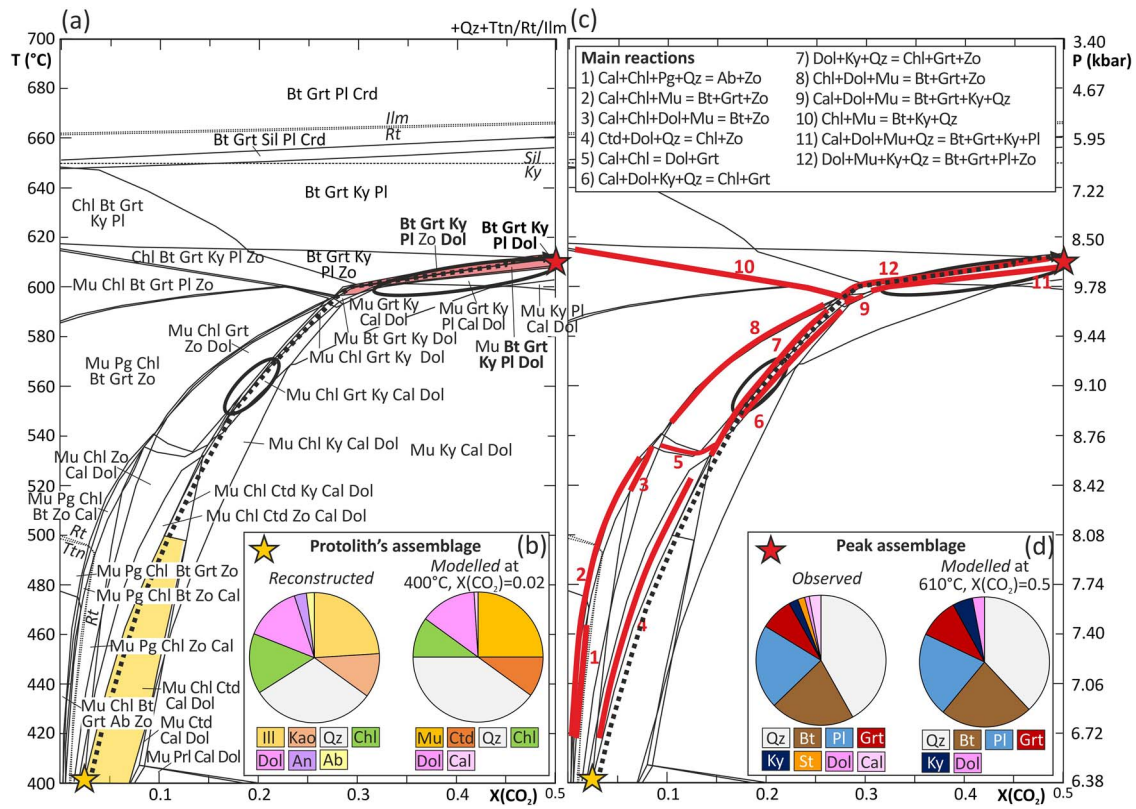
Fig. 9. (a) P/T-X(CO$_2$) mineral assemblage diagram modelled for sample 17a-29. The variance of the fields varies from two (i.e. nine phases) to five (i.e. six phases). Colours and symbols as in Fig. 8. (b) Comparison between the reconstructed protolith assemblage and that modelled at the 'starting point'. (c) Same plot as (a), highlighting the isothermal/isobaric univariant equilibria relevant to this sample. Colours and symbols as in Fig. 8. (d) Comparison between the observed peak assemblage and that modelled at peak conditions. The black ellipses and dotted black arrows in (a) and (c) summarise the prograde and peak conditions and approximate the P–T–X(CO$_2$) evolution inferred for sample 17a-29 as discussed in the text.

Sample 18a-26. The observed peak assemblage (Qz + Dol + Bt + Pl + Ky) is modelled by a field located at T = 600–615 °C, P = 9.8–8.8 kbar, X(CO$_2$) > 0.40 (Fig. 11a). A minor amount of magnesite (<3%) is predicted in this field, although not observed in the sample (Fig. 11d). The XMg and XCa compositional isopleths modelled for biotite and plagioclase, respectively, and corresponding to their measured compositions (biotite: XMg = 0.94–0.95; plagioclase: XCa = 0.45–0.69) converge at the inferred peak T-X(CO$_2$) conditions of 610 °C, X(CO$_2$) = 0.6 (Supplementary Fig. S9d). At these conditions, the observed and modelled mineral modes are in very good agreement (Fig. 11d).

Magnesite series

Following the strategy discussed above, the starting points for the P–T–X(CO$_2$) evolution of the samples belonging to the magnesite series are fixed at 400 °C and at X(CO$_2$) = 0.04 for sample 17a-36b, X(CO$_2$) = 0.07 for sample 17a-35 and X(CO$_2$) = 0.10 for sample 17b-7d. Prograde and peak conditions for each sample are defined as follows:

Sample 17a-36b. The observed peak assemblage (Qz + Bt + Mu + Pl + Ep ± Ky) is modelled by a field located at T = 600–620 °C, P = 9.8–8.5 kbar, X(CO$_2$) > 0.05 (Fig. 12a). In this field, the predicted amount of kyanite and epidote is low (<1%), in agreement with the observed assemblage (Fig. 12d). The XMg and XCa compositional isopleths modelled for biotite and plagioclase, respectively, and corresponding to their measured compositions (biotite: XMg = 0.91–0.93; plagioclase: XCa = 0.32–0.42) are consistent with these peak conditions (Supplementary Fig. S9e). The modelled mineral modes converge to the observed ones at 615 °C,

X(CO$_2$) = 0.25 (Fig. 12d), which are therefore inferred to be the peak conditions.

Sample 17a-35. Compositional isopleths modelled for the garnet core, corresponding to its measured composition (GrtC: XMg = 0.22, XCa = 0.16, XMn = 0.01), converge in the narrow field Qz + Chl + Bt + Grt + Pl + Ky + Hbl + Rt + Mgs (Fig. 13a and Supplementary Fig. S9f), constraining garnet nucleation in the prograde stage at T = 595–615 °C, P = 9–9.6 kbar. The observed peak assemblage (Qz + Bt + Ky + Grt + Oamp + Hbl ± Crd) is approximated by several fields located at T = 615–645 °C, P = 8.6–7.2 kbar, X(CO$_2$) > 0.3 (Fig. 13a). None of these fields match the observed assemblage perfectly because they contain phases that are not present in the sample (i.e. chlorite, talc or plagioclase). However, the four-variant field Qz + Bt + Grt + Ky + OAmp + Hbl + Tlc comes closest to the observed peak assemblage, being able to reproduce the coexistence of hornblende and ortho-amphibole, as well as the observed proportions of kyanite and biotite (Fig. 13d). According to these results, cordierite is a later phase, which is in any case compatible with a decompression evolution (Fig. 13a). Compositional isopleths modelled for the post-kinematic garnet rim (GrtR: XMg = 0.32, XCa = 0.12, XMn = 0.003) further constrain its growth at T = 615–640 °C, P = 8.5–7.2 kbar (Supplementary Fig. S9f). Compositional isopleths of the other post-kinematic phases in equilibrium with the garnet rim, i.e. biotite, hornblende and orthoamphibole (Bt: XMg = 0.73–0.78; Hbl: XMg = 0.8–0.82; OAmp: XMg = 0.65–0.71), intersect at the same P–T interval (Supplementary Fig. S9f), confirming that the peak assemblage developed during the decompression stage.
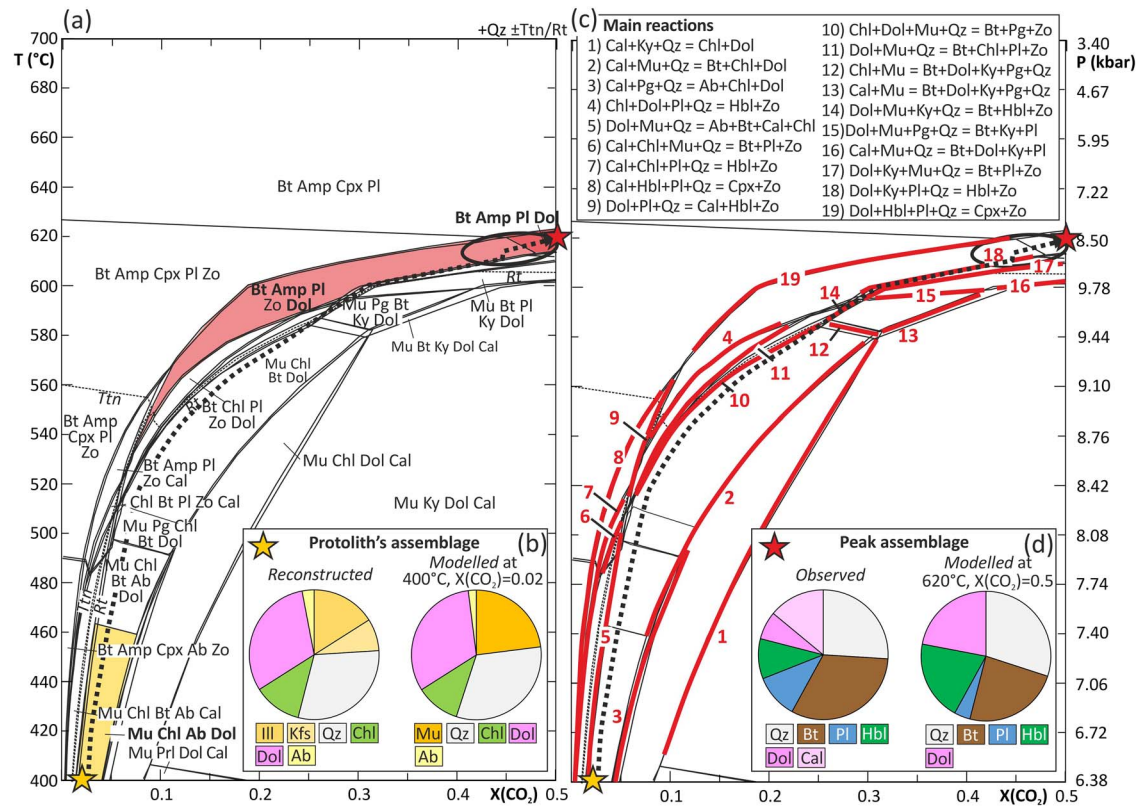
Fig. 10. (a) P/T-X(CO$_2$) mineral assemblage diagram modelled for sample 15a-28a. The variance of the fields varies from two (i.e. eight phases) to five (i.e. five phases). Colours and symbols as in Fig. 8. (b) Comparison between the reconstructed protolith assemblage and that modelled at the 'starting point'. (c) Same plot as (a), highlighting the isothermal/isobaric univariant equilibria relevant to this sample. Colours and symbols as in Fig. 8. (d) Comparison between the observed peak assemblage and that modelled at peak conditions. The black ellipses and dotted black arrows in (a) and (c) summarise the prograde and peak conditions and approximate the P–T–X(CO$_2$) evolution inferred for sample 15a-28a as discussed in the text.

Sample 17b-7d. The observed peak assemblage (Mgs + Tlc + Chl) is modelled by a large four-variant field extending from the prograde stage (T > 500 °C, X(CO$_2$) < 0.1) to the decompression stage (T < 650 °C, X(CO$_2$) < 0.6) (Fig. 14a). Compositional isopleths of the peak phases do not help to further constrain the peak conditions, as all phases are close to the pure end-member compositions. Instead, the modelled isomodes for magnesite, talc and chlorite (Supplementary Fig. S9g), corresponding to the measured modal amount of each phase (Mgs 74%, Tlc 12%, Chl 14%), constrain the peak P–T–X(CO$_2$) conditions at c. 630 °C, 8.0 kbar, X(CO$_2$) = 0.15 (Fig. 14d).

DISCUSSION
P–T–X(CO$_2$) evolution and decarbonation processes in dolomitic and magnesitic lithologies

For most samples, the phase diagram modelling results strongly suggest that equilibrium mineral assemblages buffered the pore fluid composition during most of the metamorphic evolution. Indeed, most of the observed prograde and peak mineral assemblages are modelled in equilibrium with a fluid characterised by an X(CO$_2$) value systematically higher than that of the fluid in equilibrium with the protolith assemblage (i.e. at the 'starting point'). It is therefore unlikely that this behaviour is due to the infiltration of external fluids. Internally buffered behaviour is common during prograde metamorphism of silicate–carbonate rocks (Greenwood, 1975; Baker et al., 1991), as confirmed by several independent petrological evidences (e.g. Connolly & Trommsdorff, 1991; Groppo et al., 2017, 2021; Rapa et al., 2017;

Eberhard & Pettke, 2021). It has been shown that as long as a system remains internally buffered, the sudden and volumetrically significant appearance of new phases and the simultaneous disappearance of previously abundant phases occur at the isobaric/isothermal invariant points, whereas modal changes along the univariant curves are only minor (e.g. Greenwood, 1975; Groppo et al., 2017). In contrast, univariant reactions lead to the volumetrically significant appearance of new phases when the buffering capacity of the system is exhausted due to the complete consumption of one or more reactants. Most of the following discussion is based on the assumption of internally buffered behaviour. The exception is sample 17b-7d (magnesite + talc rock), for which the peak conditions are inferred at an X(CO$_2$) value very similar to that of the fluid in equilibrium with the protolith assemblage (Fig. 14a). This suggests an externally buffered evolution for this sample, controlled by the infiltration of externally derived fluids.

The following discussion summarises the P–T–X(CO$_2$) evolution inferred for each sample, focusing on the major decarbonation reactions that occurred during the prograde and/or decompression stages and on the amounts of CO$_2$ released. Details on how the P–T–X(CO$_2$) evolution was reconstructed are provided in the Supplementary Material.

Dolomite series

Sample 17b-12. Based on the P–T–X(CO$_2$) evolution reconstructed for sample 17b-12 (see the Supplementary Material), the following points can be highlighted: (i) the most significant decarbonation reaction occurs during the prograde evolution (reaction 3 in
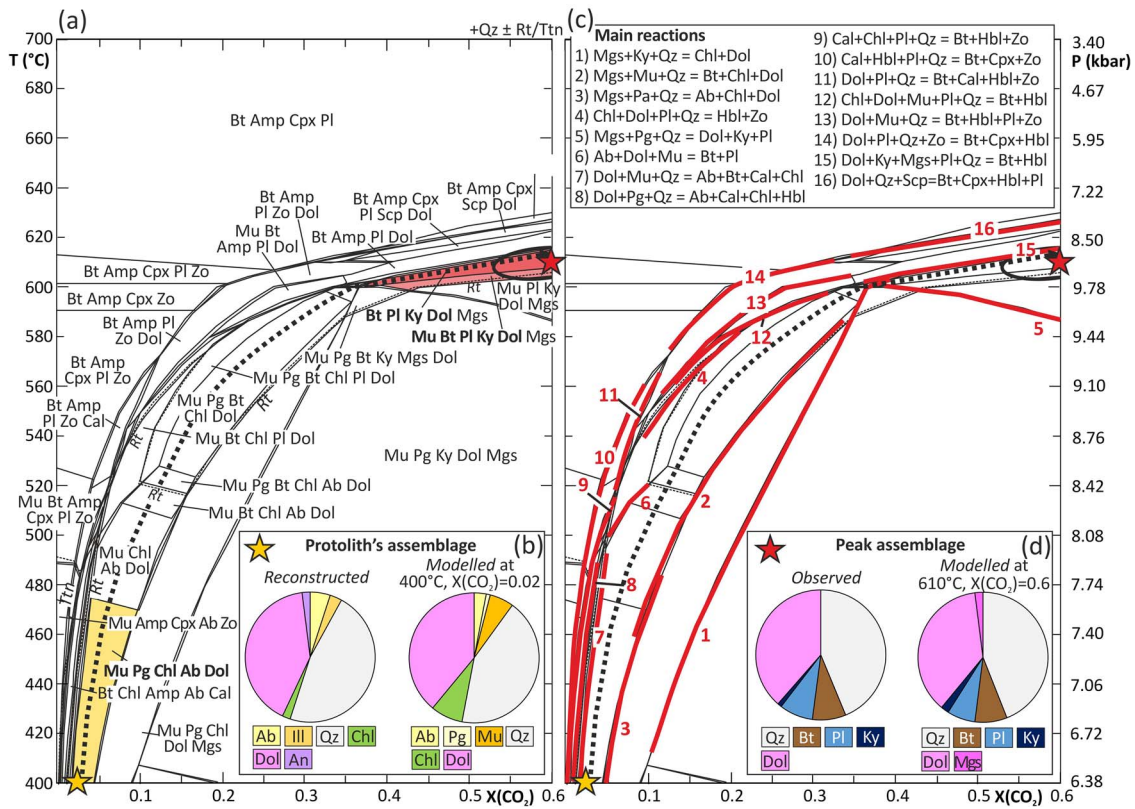
Fig. 11. (a) P/T-X(CO$_2$) mineral assemblage diagram modelled for sample 18a-26. The variance of the fields varies from two (i.e. eight phases) to five (i.e. five phases). Colours and symbols as in Fig. 8. (b) Comparison between the reconstructed protolith assemblage and that modelled at the 'starting point'. (c) Same plot as (a), highlighting the isothermal/isobaric univariant equilibria relevant to this sample. Colours and symbols as in Fig. 8. (d) Comparison between the observed peak assemblage and that modelled at peak conditions. The black ellipses and dotted black arrows in (a) and (c) summarise the prograde and peak conditions and approximate the P–T–X(CO$_2$) evolution inferred for sample 18a-26 as discussed in the text.

Fig. 8c: Chl + Dol + Mu + Qz = Bt + Ep), in the temperature interval 450–560 °C, and is responsible for the final consumption of dolomite. The absence of dolomite relics in the sample can be explained either by the low amounts of dolomite initially present in the protolith and/or by the fact that the main product of this decarbonation reaction is biotite, which is not a favourable host mineral for preserving carbonate relics during metamorphism. An additional decarbonation reaction is predicted at higher temperatures (540–580 °C), which leads to the consumption of a very small amount of magnesite (0.2 vol%), and is therefore irrelevant for the overall estimate of the CO$_2$ budget; (ii) the fluid produced by the main decarbonation reaction has X(CO$_2$) = 0.05–0.20 (Fig. 8c); (iii) a total amount of dolomite of 6–8 vol% (depending on whether the modelled vs. reconstructed protolith's mode is used) is consumed by this process, corresponding to an amount of CO$_2$ produced of 3.1–4.1 wt%.

Sample 17a-29. From the reconstructed P–T–X(CO$_2$) evolution (see the Supplementary Material), the following points can be highlighted: (i) most decarbonation occurs during the decompression stage, at T > 610 °C, by an almost discontinuous reaction (reaction 12, Fig. 9c: Dol + Mu + Ky + Qz = Bt + Grt + Pl + Zo) responsible for the consumption of a relatively large amount of dolomite (11 vol%). The observed relict carbonate inclusions within garnet and plagioclase (Fig. 4f, g) are consistent with the modelled reaction. This decarbonation event is preceded by a minor episode of carbonate consumption (reaction 6, Fig. 9c), which occurs during the prograde evolution at 550–570 °C; this reaction is responsible for the decomposition of a small amount of calcite (<1 vol%) and is therefore irrelevant for the overall esti-

mate of the CO$_2$ budget; (ii) the fluid produced by the main decarbonation reaction is enriched in CO$_2$, with X(CO$_2$) ≥ 0.5 (Fig. 9c); (iii) at the end of the modelled P–T–X(CO$_2$) evolution, a total amount of dolomite of about 11 vol% is consumed by this process, corresponding to an amount of CO$_2$ produced of 5.6 wt%.

Sample 15a-28a. Based on the reconstructed P–T–X(CO$_2$) evolution (see the Supplementary Material), it is concluded that (i) most decarbonation occurs by a single step-like reaction during the decompression stage, at T > 610 °C (reaction 18, Fig. 10c: Dol + Ky + Pl + Qz = Hbl + Zo), consuming about one-third of the dolomite initially present in the protolith. The observed corroded inclusions of dolomite, quartz and plagioclase within porphyroblastic hornblende (Fig. 5b) are consistent with the modelled reaction; (ii) the fluid released by this decarbonation reaction has X(CO$_2$) > 0.5 (Fig. 10c); (iii) the amount of dolomite consumed by this process is about 10 vol%, corresponding to a CO$_2$ production of 5.1 wt%.

Sample 18a-26. The reconstructed P–T–X(CO$_2$) evolution (see the Supplementary Material) shows that (i) in this sample, decarbonation processes are much less significant than in the other samples of the dolomite series and occur by continuous reactions operating over large P–T–X(CO$_2$) intervals rather than by discontinuous reactions; (ii) the fluid in equilibrium with the peak assemblage has X(CO$_2$) > 0.6; (iii) according to the modelling results, 2 vol% of dolomite is consumed along this P–T–X(CO$_2$) pathway, but 2 vol% of magnesite is produced, thus maintaining the overall CO$_2$ budget. Even if no magnesite was produced (as suggested by the observed peak assemblage), the amount of CO$_2$ produced would be very small (1.0 wt%).
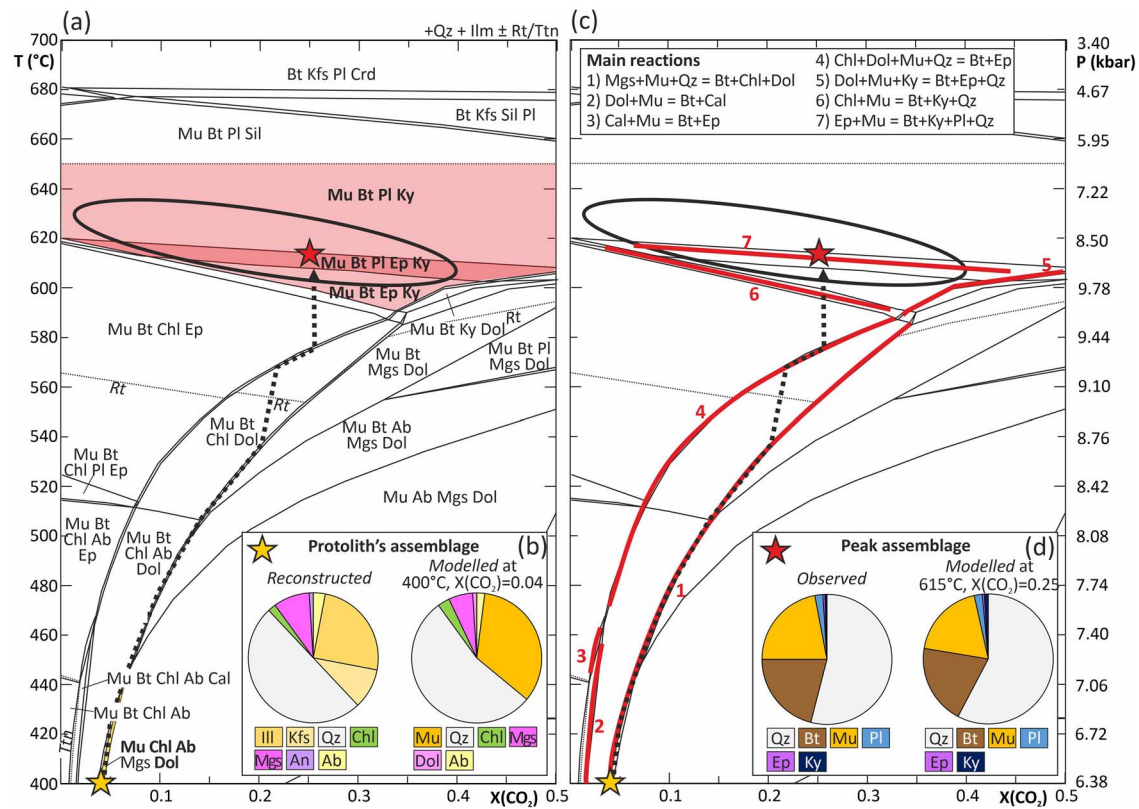
Fig. 12. (a) P/T-X(CO_2) mineral assemblage diagram modelled for sample 17a-36b. The variance of the fields varies from two (i.e. nine phases) to five (i.e. six phases). Colours and symbols as in Fig. 8. (b) Comparison between the reconstructed protolith assemblage and that modelled at the 'starting point'. (c) Same plot as (a), highlighting the isothermal/isobaric univariant equilibria relevant to this sample. Colours and symbols as in Fig. 8. (d) Comparison between the observed peak assemblage and that modelled at peak conditions. The black ellipses and dotted black arrows in (a) and (c) summarise the prograde and peak conditions and approximate the P–T–X(CO_2) evolution inferred for sample 17a-36b as discussed in the text.

Magnesite series

Sample 17a-36b. The P–T–X(CO_2) evolution reconstructed for sample 17a-36b (see the Supplementary Material) implies that (i) most decarbonation occurs via a single, step-like reaction responsible for the complete consumption of all the magnesite originally present in the protolith (reaction 1, Fig. 12c: Mgs + Mu + Qz = Bt + Chl + Dol). Although difficult to constrain precisely in terms of P, T and X(CO_2) conditions, this major episode of CO_2 production occurs during the prograde stage (T = 520–550 °C). The low amounts of magnesite initially present in the protolith could explain the absence of magnesite relics in the sample; in addition, biotite is the main product of this decarbonation reaction, which is not a favourable host mineral for preserving carbonate relics during metamorphism. A further decarbonation reaction is predicted at slightly higher temperatures (560–580 °C), which results in the consumption of a very small amount of dolomite (<0.5 vol%) and is therefore irrelevant to the overall estimate of the CO_2 budget; (ii) the fluid produced by the main decarbonation reaction has X(CO_2) = 0.1–0.2 (Fig. 12c); (iii) the amount of magnesite consumed by this process is between 6 and 9 vol%, corresponding to an amount of CO_2 produced of 3.4–5.1 wt%.

Sample 17a-35. The reconstructed P–T–X(CO_2) evolution (see the Supplementary Material) suggests that (i) two main decarbonation reactions occur during the decompression stage at T = 600–610 °C, which are responsible for the final consumption of all dolomite and magnesite initially present in the protolith (reactions 6 and 2, Fig. 13c). The magnesite-consuming, garnet-forming reaction 2 (Mgs + Ky + Qz = Chl + Grt) is the most relevant in terms

of CO_2 production, as it leads to the consumption of 17–18 vol% of magnesite, compared to 2–3 vol% of dolomite consumed by reaction 6 (Dol + Ky + Mgs + Pl = Hbl + Qz). The observed rare relics of dolomite within Ca-amphibole are consistent with the modelled reaction (6). In spite of the careful search, magnesite relics have not been found in garnet, possibly due to its rapid growth; (ii) the fluid produced by these decarbonation reactions is quite enriched in CO_2, with X(CO_2) values ranging between 0.3 and 0.4; (iii) the amount of CO_2 produced by the decomposition of 2–3 vol% dolomite and 17–18 vol% magnesite is 1.0–1.5 wt% and 9.7–10.3 wt%, respectively.

Sample 17b-7d. This sample differs from the others discussed so far in that the predicted X(CO_2) of the fluid in equilibrium with the peak assemblage is very similar to that of the fluid modelled at the 'initial' P–T–X(CO_2) conditions (Fig. 14a). This implies that the sample has followed an almost vertical P–T–X(CO_2) evolution, which is typical of externally buffered systems where the composition of the fluid is controlled by the infiltration of external fluids rather than by the system itself. According to the results of the modelling (see the Supplementary Material), the following points are worth mentioning: (i) the sample undergoes two major decarbonation events during the prograde stage (reactions 1 and 3, Fig. 14c: Mgs + Prl = Chl + Qz; Mgs + Qz = Tlc), each responsible for the consumption of 5–6 vol% magnesite. The observed Mg-chlorite and talc replacing magnesite crystals at their rims (Fig. 7c, d and Fig. S6 in the Supplementary Material) are consistent with both modelled reactions (see also Brady *et al.*, 1998 for similar microstructures and interpretation). These decarbonation reactions are modelled at around 405–410 °C and
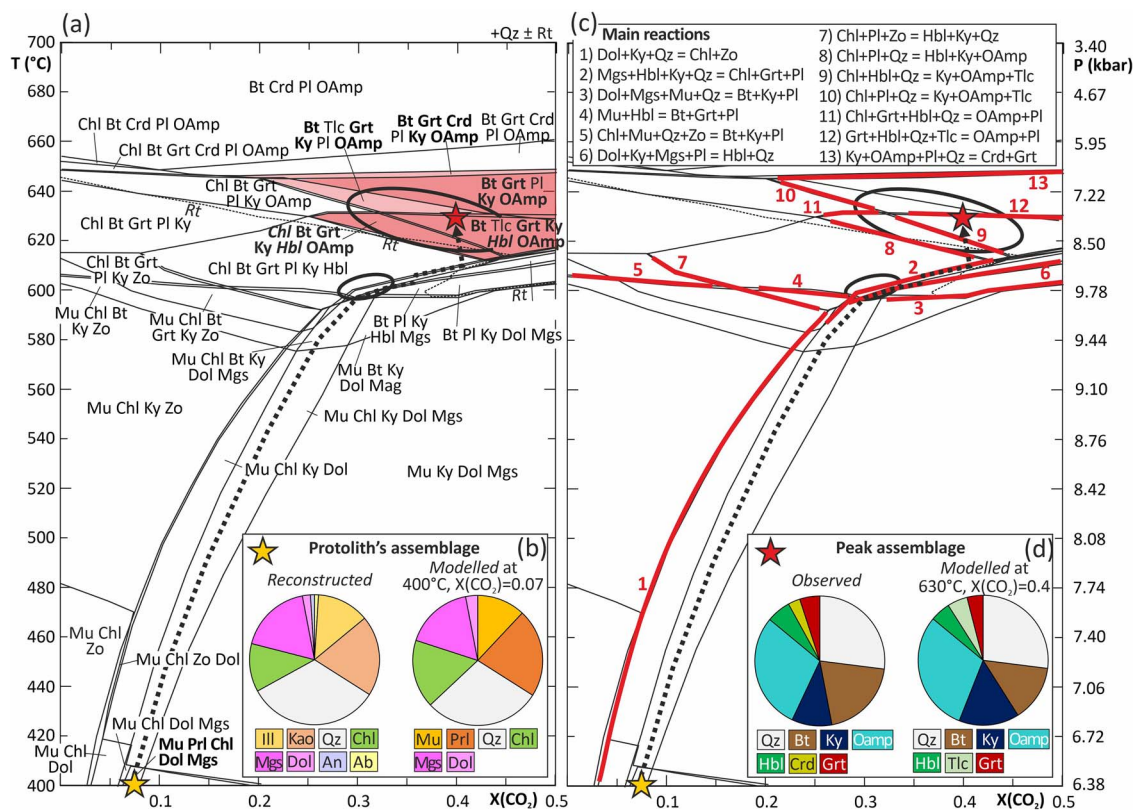
Fig. 13. (a) P/T-X(CO_2) mineral assemblage diagram modelled for sample 17a-35. The variance of the fields varies from two (i.e. nine phases) to five (i.e. six phases). Colours and symbols as in Fig. 8. (b) Comparison between the reconstructed protolith assemblage and that modelled at the 'starting point'. (c) Same plot as (a), highlighting the isothermal/isobaric univariant equilibria relevant to this sample. Colours and symbols as in Fig. 8. (d) Comparison between the observed peak assemblage and that modelled at peak conditions. The black ellipses and dotted black arrows in (a) and (c) summarise the prograde and peak conditions and approximate the P–T–X(CO_2) evolution inferred for sample 17a-35 as discussed in the text.

480–500 °C, respectively, and are triggered by the influx of H_2O-rich external fluids, probably originating from the metapelites hosting the lenticular bodies of magnesite-rich ores; (ii) the fluid produced by these decarbonation reactions has low X(CO_2) values; (iii) the amount of CO_2 produced by the decomposition of 5–6 vol% magnesite is 2.8–3.4 wt% for each of the two CO_2-producing pulses, for a total CO_2 production of 5.6-6.9 wt%.

CO_2 productivity of the different dolomitic and magnesitic lithologies

The results of the thermodynamic modelling show that, for all samples studied, decarbonation occurs in one—or more—pulses through nearly discontinuous reactions operating at relatively narrow temperature intervals, rather than being a continuous process during most of the prograde evolution. The main decarbonation reactions inferred for the studied samples can be classified into two groups, based on the nature of mineral reactants and products: (1) reactions among a carbonate (dolomite or magnesite), muscovite and quartz (± additional Al-rich silicates), producing biotite in equilibrium with Ca-rich silicates (dolomite series) or Mg-rich silicates (magnesite series); (2) reactions among a carbonate (dolomite or magnesite), quartz and kyanite, producing Ca-rich silicates in samples from the dolomite series, or Mg-rich silicates in samples from the magnesite series. Reactions of group (1) are the main decarbonation reactions in samples originally containing low amounts of carbonate and high amounts of illite (i.e. illite/carbonate ratio > 1.5–2.0%), i.e. samples 17b-12 (Dol+Mu+Qz+Chl=Bt+Ep), 17a-29 (Dol+Mu+Qz+Ky=Bt+Grt+Pl+Zo), 17a-36b (Mgs+Mu+Qz=

Bt+Chl+Dol), and mostly occur at relatively low temperature, during the prograde stage. Reactions of group (2) characterise the samples originally containing moderate amounts of carbonate and lower amounts of illite (i.e. illite/carbonate ratio < 1.5–2.0%), i.e. samples 15a-28a (Dol+Qz+Ky+Pl=Hbl+Zo), 17a-35 (Mgs+Qz+Ky=Chl+Grt), and occur at higher temperatures (T > 600°C), during the decompression stage. This implies that the most significant episode of decarbonation in each sample occurs at progressively higher temperatures for decreasing illite/carbonate ratios in the protolith. The original abundance of illite in the protolith is likely the most important factor that influences the temperature of decarbonation, being directly related to the amount of muscovite (i.e. the most efficient reactant) formed at the onset of prograde metamorphism.

The carbonate content of the protolith also influences the final amount of CO_2 released by each lithology (see e.g. Yardley, 1997, for similar conclusions), but the relationship between these two parameters is not linear (Fig. 15). For the dolomite series, the results of the fitting show that (i) samples derived from protoliths originally containing 15–40% dolomite produce the largest amounts of CO_2, in the range 5.5 ± 1.0 – 7.1 ± 1.5 wt% CO_2 (Table 3 and Fig. 15a), whereas (ii) dolomitic pelites originally containing less than 10% dolomite and (iii) dolomitic marls originally containing 40–50% dolomite are less productive (<4 ± 0.6 wt% CO_2); (iv) dolomitic marbles derived from impure dolostones originally containing more than 70% dolomite are essentially unreactive. Overall, the CO_2 produced as a function of the amount of carbonate originally present in the protolith is similar to that estimated for calcite-bearing sediments metamorphosed under high
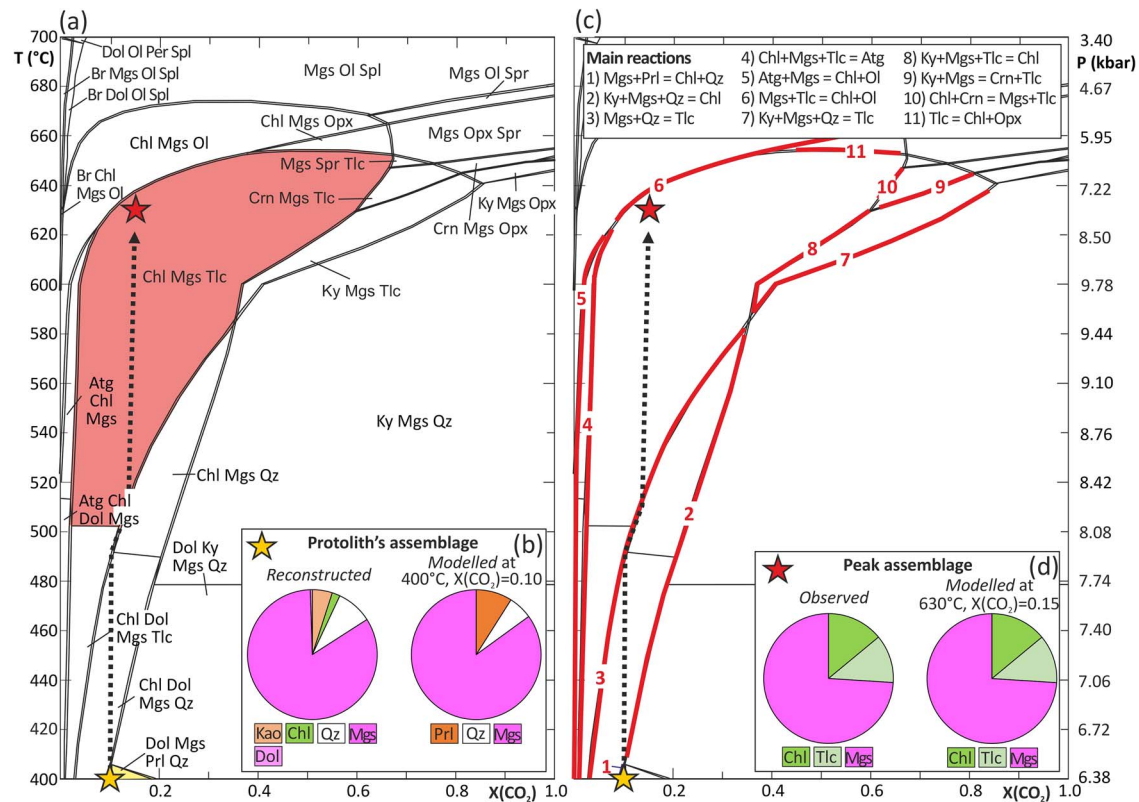
Fig. 14. (a) P/T-X(CO$_2$) mineral assemblage diagram modelled for sample 17b-7d. The variance of the fields varies from two (i.e. five phases) to four (i.e. three phases). Colours and symbols as in Fig. 8. (b) Comparison between the reconstructed protolith assemblage and that modelled at the 'starting point'. (c) Same plot as (a), highlighting the isothermal/isobaric univariant equilibria relevant to this sample. Colours and symbols as in Fig. 8. (d) Comparison between the observed peak assemblage and that modelled at peak conditions. The black ellipses and dotted black arrows in (a) and (c) summarise the prograde and peak conditions and approximate the P–T–X(CO$_2$) evolution inferred for sample 17b-7d as discussed in the text.

geothermal gradients (Groppo *et al.*, 2017, 2021, 2022; Rapa *et al.*, 2017), both in terms of trend and absolute values (Fig. 15c, d).

Similarly for the magnesite series, the samples derived from magnesitic marls with more than 15% magnesite are the most productive ($7.5 \pm 0.9 – 10.5 \pm 1.5$ wt% CO$_2$), whereas magnesitic pelites that originally contained less than 10% magnesite release lower amounts of CO$_2$ (<5 ± 0.5 wt% CO$_2$; Table 3 and Fig. 15b). In terms of absolute values, magnesite-bearing protoliths produce up to 40% more CO$_2$ than dolomite and calcite-bearing pelites and marls (Fig. 15d). Samples derived from protoliths dominated by magnesite (i.e. magnesite ores, with Mgs > 75%) apparently have an opposite behaviour with respect to impure dolostones and limestones, being reactive during the prograde stage and releasing quite significant amounts of CO$_2$. However, this behaviour is strictly related to the availability of external H$_2$O-rich fluids, which infiltrated the magnesite ores. Field observations suggest that where the influx of external fluids was nil or negligible, little or no talc developed at the expense of magnesite and the magnesitic body remained essentially unreactive (Supplementary Figs S1f and S6a–f). Conversely, where external fluid infiltration was pervasive (e.g. in the case of thin, metric layers of magnesitic rocks embedded in metapelites), most of the original magnesite was replaced by talc and the rock was transformed into a talc schist (Supplementary Figs S1h and S6g, h). Consequently, the amounts of CO$_2$ potentially released by magnesite ores vary dramatically from zero (in the case of no infiltration) to extremely high values when most of the magnesite is converted to talc.

These results show that the CO$_2$ productivity of dolomitic and magnesitic pelites and marls is significant, at least in terms of CO$_2$

produced at depth, and is similar to, or even higher than, that of calcareous pelites and marls *sensu stricto* (Fig. 15d). Irrespective of the type of carbonate in the protolith, the maximum CO$_2$ production is systematically recorded by sediments originally containing 15–40% carbonate, whereas for carbonate contents above 60–70% CO$_2$, productivity is negligible, unless aqueous fluids infiltrate from the outside and trigger decarbonation reactions. Depending on the ability of the CO$_2$-rich fluids to ascend to the Earth's surface without interacting with the host rocks (Groppo *et al.*, 2022), dolomitic and magnesitic lithologies, which are quite abundant in the Upper-LHS, could be relevant sources of CO$_2$, possibly contributing to the diffuse Himalayan CO$_2$ degassing currently observed at the surface (e.g. Girault *et al.*, 2014, 2018, 2023a, 2023b).

Evaporitic protoliths in the LHS metasedimentary sequence

The peculiar mineral assemblages and compositions observed in some of the samples studied stimulate a wider discussion on the nature of their protoliths, with potential implications for the reconstruction of their depositional environments. Sample 17a-35, belonging to the magnesite series, is particularly interesting for its unusual assemblage (phlogopite + orthoamphibole + kyanite + garnet + cordierite + quartz), reflecting the high amounts of MgO, Al$_2$O$_3$ and K$_2$O in its bulk-rock composition, offset by low amounts of CaO. Although unusual in the Upper-LHS metasedimentary sequence of Central Nepal, its occurrence is not unique; similar lithologies have been collected in the nearby region, which can be described as phlogopite + kyanite + orthoamphibole + plagioclase
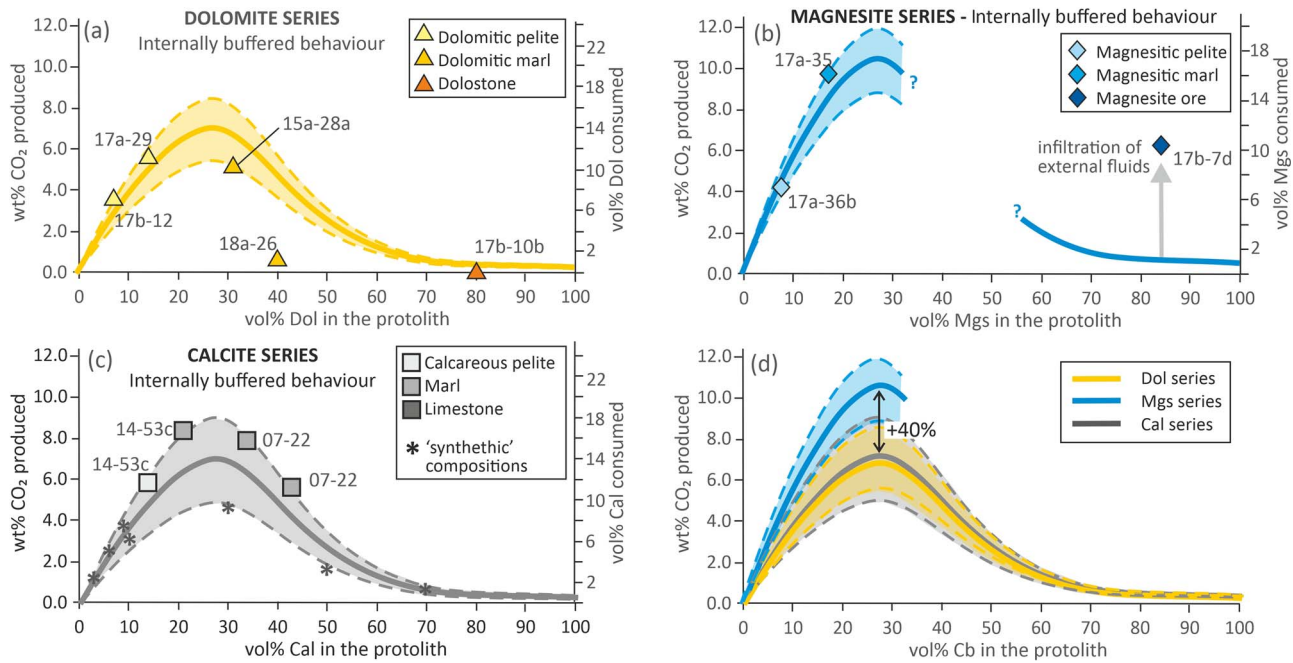
Fig. 15. Diagrams showing the amount of CO_2 produced as a function of the initial amount of carbonate originally present in the protolith for the dolomite (a), magnesite (b) and calcite (c) series and comparison of the CO_2 productivities among the three series (d). Punctual data for the dolomite (triangles) and magnesite (diamonds) series derive from this study, whereas those for the calcite series (squares) are from Rapa *et al.* (2017) (samples 14-53c, two points for calcite-poor and calcite-rich layers), Groppo *et al.* (2017) (sample 07-22, two points for calcite-poor and calcite-rich layers), Groppo *et al.* (2021) (Cal3, Cal6, Cal9 'synthetic' compositions) and Groppo *et al.* (2022) (Cal10, Cal30, Cal50, Cal70 'synthetic' compositions). It appears that the most productive lithologies in terms of CO_2 released are carbonatic pelites and marls containing 15–40% carbonates. Note that sample 18a-26 in (a), which is outside the average trend for the dolomite series, is from a protolith extremely enriched in quartz and very poor in clay minerals (Fig. S2, Supplementary Material).

Table 3: Amounts of CO_2 produced by different lithologies from the Nepal Himalaya

Sample	vol% Cb in protolith	vol% Cb consumed		wt% CO_2 produced		Reference
		(A)	(B)	(A)	(B)	
Dolomite series						
17b-12	7	6 ± 0.7	7	2.9 ± 0.4	3.6	This study
17a-29	14	10 ± 1.7	11	5.2 ± 0.9	5.6	This study
15a-28a	31	14 ± 2.9	10	6.9 ± 1.4	5.1	This study
18a-26*	40	10 ± 2.0	1	5.3 ± 0.9	0.5	This study
17b-10b	80	1 ± 0.04	0	0.6 ± 0.02	0	This study
Magnesite series						
17a-36b	7.5	7 ± 0.5	7.5	3.9 ± 0.3	4.2	This study
17a-35	17	15 ± 1.7	17	8.5 ± 1.0	9.7	This study
17b-7d§	84	1 ± 0.01	11	0.6 ± 0.01	6.2	This study
Calcite series						
'Synthetic' Cal3	3	3 ± 0.4	3	1.2 ± 0.2	1.2	Rapa *et al.* (2017)
'Synthetic' Cal6	6	5 ± 0.8	6	2.3 ± 0.4	2.5	Rapa *et al.* (2017)
'Synthetic' Cal9	9	8 ± 1.7	9	3.4 ± 0.7	3.7	Groppo *et al.* (2017)
'Synthetic' Cal10	10	9 ± 1.9	7.5	3.7 ± 0.8	3.1	Groppo *et al.* (2017)
14-53c (Cal-poor)	14	12 ± 2.8	14	5.0 ± 1.1	5.9	Groppo *et al.* (2021)
14-53c (Cal-rich)	21	16 ± 4.2	20	6.5 ± 1.8	8.4	Groppo *et al.* (2021)
'Synthetic' Cal30	30	16 ± 4.6	12	6.8 ± 1.9	4.6	Groppo *et al.* (2021)
07–22 (Cpx-rich)	34	15 ± 4.1	19	6.3 ± 1.7	8.0	Groppo *et al.* (2022)
07–22 (Cal-rich)	43	10 ± 2.3	14	4.3 ± 0.9	5.9	Groppo *et al.* (2022)
'Synthetic' Cal50	50	7 ± 1.1	4	2.8 ± 0.4	1.6	Groppo *et al.* (2022)
'Synthetic' Cal70	70	2 ± 0.1	1.5	0.7 ± 0.1	0.6	Groppo *et al.* (2022)

(A) Average values inferred from the non-linear fitting of punctual data. (B) Punctual data constrained from the phase diagram modelling. *Note that sample 18a-26 derives from a protolith extremely enriched in quartz and very poor in clay minerals, which explains its deviation from the average behaviour of the dolomite series. §Note that an externally buffered behaviour has been inferred for sample 17b-7d, which explains its deviation from the average behaviour of the magnesite series.

talc schist, kyanite + hornblende + orthoamphibole chlorite-phlogopite schist, and orthoamphibole-bearing chlorite-talc schist. These assemblages have a strong affinity with those described for cordierite-orthoamphibole gneisses from various localities worldwide, the origin of which is still debated (e.g. Diener et al., 2008). A widely accepted hypothesis is that the protoliths of cordierite-orthoamphibole-bearing gneisses are mafic rocks metasomatised in seafloor hydrothermal systems (e.g. Chinner & Fox, 1974; Moore & Waters, 1990; Smith et al., 1992; Pan & Fleet, 1995; Roberts et al., 2003; Peck & Smith, 2005), which may also explain the common association of these lithologies with massive sulphide deposits. However, this hypothesis is difficult to support when these rocks are exposed in metasedimentary sequences that are devoid of mafic rocks and instead dominated by carbonate-bearing lithologies. In such a context, isochemical metamorphism of rocks with unusual bulk compositions, such as evaporite-bearing sedimentary rocks, is a reliable alternative to explain the origin of cordierite-orthoamphibole-bearing gneisses (e.g. Kulke & Schreyer, 1973; Moine et al., 1981; Reinhardht, 1987). Our data support this second hypothesis; i.e. samples belonging to the magnesite series are likely to have been derived from evaporitic sediments. While the evaporitic origin of magnesite ore deposits has been well documented throughout the Himalayan belt (e.g. Valdiya, 1995; Joshi & Sharma, 2015), this is the first report of the former occurrence of magnesite-bearing protoliths (i.e. magnesitic pelites, magnesitic marls) of possible evaporitic origin within the Upper-LHS metasedimentary sequence.

Metamorphosed evaporite-bearing sedimentary sequences have been described in various orogenic belts on all the continents, from Africa (e.g. Zambian Copperbelt: Moine et al., 1981; Zambesi Orogenic Belt: Hanson et al., 1994) to Australia (e.g. Southern Australia: Cook & Ashley, 1992; Northern Australia: Reinhardht, 1987; Oliver, 1995; Morissey & Tomkins, 2020), Asia (e.g. Himalayan orogen: Schryer & Abraham, 1976; Faryad, 2002; Garnier et al., 2008; North China Craton: Dong et al., 2016), America (e.g. Grenville Province, North America: Hogarth & Griffin, 1978; Gresens, 1978; Rich, 1979; Peck & Eppich, 2019; Oaxacan granulite complex, Mexico: Ortega-Gutierrez, 1984; Paranoa Group, Brazil: Leake & Farrow, 1979; Giuliani et al., 1993; Colombia: Giuliani et al., 2000) and Europe (e.g. Seve Nappe Complex, Sweden: Svenningsen, 1994; Betic Cordilleras, Spain: Torres, 1978). Common features of these evaporite-bearing metasedimentary sequences are (i) their Proterozoic age, (ii) the systematic association with different types of stratabound metallic mineral deposits, including Pb–Zn–(Ag) and Cu–Fe sulphide deposits, and banded iron formations (Eugster & Chou, 1973; Walker et al., 1977; Neudert & Russell, 1981; Eugster, 1985; Kucha & Pawlikowski, 1986; Haynes, 1986a, 1986b; Jowett et al., 1987; Warren, 1997, and references therein) and (iii) the association with gemstone-bearing lithologies and/or gems, such as rubies, emeralds and lapis lazuli (e.g. Giuliani et al., 2000; Faryad, 2002; Garnier et al., 2008, and references therein). Magnesite deposits have also been reported from some of these metamorphosed evaporite-bearing sequences (e.g. Prochaska & Krupenin, 2013; Peck & Eppich, 2019). The genetic relation between these evaporitic sequences and base metal deposits and gemstone-bearing lithologies has been explained by Warren (1997) and Garnier et al. (2008).

In the Ganesh Himal region of Central Nepal, about 10 km eastward of samples 17a-35 and 17a-36, stratabound Pb–Zn sulphide deposits are exposed in the Upper-LHS sequence (Chakrabarti et al., 2004), where they are associated with dolomitic marble layers that locally host ruby deposits (Garnier et al., 2008). Magnesite ores are exposed at several localities in the Kharidunga region, where the largest magnesite + talc deposit was exploited for decades (Dahal & Adhikary, 2001). Although it is not possible at this stage to definitively demonstrate a genetic link between the studied magnesitic lithologies and the Pb–Zn and ruby deposits of the Ganesh Himal region, these evidences taken together support the interpretation that the entire Upper-LHS metasedimentary sequence represents the metamorphic product of a carbonate–evaporite–pelite sequence deposited on the passive margin of the Indian Plate during the Proterozoic.

CONCLUSIONS

In this study, we have investigated the nature and metamorphic evolution of various metasediments exposed in the upper part of the LHS, Central Nepal, using a bottom-up approach, i.e. starting from the protoliths (reconstructed from bulk-rock compositions) to understand the metamorphic products. We have shown that the samples studied were derived from dolomitic and magnesitic protoliths that originally contained variable amounts of carbonates, ranging from less than 10% to more than 80%. Forward thermodynamic modelling successfully predicts the observed mineral assemblages and compositions at peak conditions, and allows constraining the P–T–$X(CO_2)$ evolution of the studied samples, as well as the main decarbonation reactions and the amounts of CO_2 produced.

This study represents a major advance for the identification of CO_2 source rocks and the evaluation of their CO_2 productivity in the LHS and has clear implications for the estimation of the Himalayan CO_2 emission budget. Indeed, we have shown that the CO_2 productivity of dolomitic and magnesitic lithologies metamorphosed during the Himalayan collision is relevant, similar to or even higher than that of calcareous lithologies, with maximum CO_2 production systematically recorded by sediments originally containing 15–40% dolomite or magnesite. Dolomitic and magnesitic lithologies are abundant in the LHS, which is currently being metamorphosed at depth beneath the Himalayan orogenic front; therefore, our results provide a key to link the diffuse CO_2 degassing currently observed at the surface along the entire Himalayan belt to the decarbonation processes occurring at depth today. The fact that massive degassing has been observed along the footwall of the MCT (Girault et al., 2014, 2018) is now explained, while contributions from deeper sources from GHS rocks (Groppo et al., 2017, 2022; Rapa et al., 2017; Rolfo et al., 2017) are likely to be significant. Further perspectives of this study that are worth to be explored in the future include (i) the identification of areas where CO_2 degassing at the surface can be expected, based on the presence of massive source rocks at depth; and (ii) the investigation of the $\delta^{13}C$ signature of different types of CO_2 source rocks (i.e. calcite, dolomite and magnesite series) and its comparison with the $\delta^{13}C$ of the gas currently outgassed at the surface, to understand whether it would be possible to detect the source of the gas based on its isotopic composition.

The bottom-up approach used in this study has also allowed us to propose, for the first time, that the entire Upper-LHS metasedimentary sequence may represent the metamorphic product of a Proterozoic carbonate–evaporite–pelite sequence. This hypothesis has interesting implications in a broader perspective, because evaporitic protoliths in metamorphic terrains are often associated with gemstone-bearing lithologies and/or base metal deposits, the latter being increasingly required as essential components of most clean energy technologies.

DATA AVAILABILITY

The data underlying this article are available in the article and in its online supplementary material.

SUPPLEMENTARY DATA

Supplementary data are available at *Journal of Petrology* online.

References

Ague, J. J. & Nicolescu, S. (2014). Carbon dioxide released from subduction zones by fluid-mediated reactions. *Nature Geoscience* **7**, 355–360. https://doi.org/10.1038/ngeo2143.

Auzanneau, E., Schmidt, M. W., Vielzeuf, D. & Connolly, J. A. D. (2010). Titanium in phengite: a geobarometer for high temperature eclogites. *Contributions to Mineralogy and Petrology* **159**, 1–24. https://doi.org/10.1007/s00410-009-0412-7.

Baker, J., Holland, T. J. B. & Powell, R. (1991). Isograds in internally buffered systems without solid solutions: principles and examples. *Contributions to Mineralogy and Petrology* **106**, 170–182. https://doi.org/10.1007/BF00306432.

Becker, J. A., Bickle, M. J., Galy, A. & Holland, T. J. B. (2008). Himalayan metamorphic CO_2 fluxes: quantitative constraints from hydrothermal springs. *Earth and Planetary Science Letters* **265**, 616–629. https://doi.org/10.1016/j.epsl.2007.10.046.

Beinlich, A., Mavromatis, V., Austrheim, H. & Oelkers, E. H. (2014). Inter-mineral Mg isotope fractionation during hydrothermal ultramafic rock alteration – implications for the global Mg-cycle. *Earth and Planetary Science Letters* **392**, 166–176. https://doi.org/10.1016/j.epsl.2014.02.028.

Bhowmik, S. K., Dasgupta, S., Hoernes, S. & Bhattacharya, P. K. (1995). Extremely high-temperature calcareous granulites from the eastern Ghats, India: evidence for isobaric cooling, fluid buffering, and terminal channelized fluid flow. *European Journal of Mineralogy* **7**, 689–704. https://doi.org/10.1127/ejm/7/3/0689.

Bickle, M. J. (1996). Metamorphic decarbonation, silicate weathering and the long-term carbon cycle. *Terra Nova* **8**, 270–276. https://doi.org/10.1111/j.1365-3121.1996.tb00756.x.

Bowen, N. L. (1940). Progressive metamorphism of siliceous limestones and dolomite. *The Journal of Geology* **48**, 225–274. https://doi.org/10.1086/624885.

Bowman, J. R. & Essene, E. J. (1982). P-T-X(CO2) conditions of contact metamorphism in the black Butte aureole, Elkhorn, Montana. *American Journal of Science* **282**, 311–340. https://doi.org/10.2475/ajs.282.3.311.

Brady, J. B., Cheney, J. T., Rhodes, A. L., Vasquez, A., Green, C., Duvall, M., Kogut, A., Kaufman, L. & Kovaric, D. (1998). Isotope geochemistry of Proterozoic talc occurrences in Archean marbles of the Ruby Mountains, Southwest Montana, U.S.A. *Geological Materials Research* **1**, 1–41.

Carmichael, D. M. (1991). Univariant mixed-volatile reactions: pressure–temperature phase diagrams and reaction isograds. *Canadian Mineralogist* **29**, 741–754.

Cartwright, I., Buick, I. S. & Harley, S. L. (1997). Timing and mechanisms of carbon isotope exchange in granulite-facies calc-silicate boudins, Rauer group, East Antarctica. *American Mineralogist* **82**, 392–404. https://doi.org/10.2138/am-1997-3-417.

Castelli, D. (1991). Eclogitic metamorphism in carbonate rocks: the example of impure marbles from the Sesia-Lanzo zone, Italian Western Alps. *Journal of Metamorphic Geology* **9**, 61–77. https://doi.org/10.1111/j.1525-1314.1991.tb00504.x.

Castelli, D., Rolfo, F., Groppo, C. & Compagnoni, R. (2007). Impure marbles from the UHP Brossasco–Isasca unit (Dora–Maira massif, western Alps): evidence for Alpine equilibration in the diamond stability field and evaluation of the X(CO2) fluid evolution. *Journal of Metamorphic Geology* **25**, 587–603. https://doi.org/10.1111/j.1525-1314.2007.00716.x.

Cesare, B., Meli, S., Nodari, L. & Russo, U. (2005). Fe^{3+} reduction during biotite melting in graphitic metapelites: another origin of CO_2 in granulites. *Contributions to Mineralogy and Petrology* **149**, 129–140. https://doi.org/10.1007/s00410-004-0646-3.

Chakrabarti, C. K., Upreti, B. N. & Ghosh, A. K. (2004). Geochemistry of the Ganesh Himal zinc-lead deposits, Central Nepal Himalaya. *Journal of Nepal Geological Society* **30**, 39–54. https://doi.org/10.3126/jngs.v30i0.31679.

Chinner, G. A. & Fox, J. S. (1974). The origin of cordierite–anthophyllite rocks in the Land's end aureole. *Geological Magazine* **111**, 397–408. https://doi.org/10.1017/S0016756800039959.

Coggon, R. & Holland, T. J. B. (2002). Mixing properties of phengitic micas and revised garnet–phengite thermobarometers. *Journal of Metamorphic Geology* **20**, 683–696. https://doi.org/10.1046/j.1525-1314.2002.00395.x.

Connolly, J. A. D. (1990). Multivariable phase diagrams: an algorithm based on generalize thermodynamics. *American Journal of Science* **290**, 666–718. https://doi.org/10.2475/ajs.290.6.666.

Connolly, J. A. D. (2009). The geodynamic equation of state: what and how. *Geochemistry, Geophysics, Geosystems* **10**, Q10014. https://doi.org/10.1029/2009GC002540.

Connolly, J. A. D. & Trommsdorff, V. (1991). Petrogenetic grids for metacarbonate rocks: pressure–temperature phase diagrams for mixed–volatile systems. *Contributions to Mineralogy and Petrology* **108**, 93–105. https://doi.org/10.1007/BF00307329.

Consuma, G., Braga, R., Giovanardi, T., Bersani, D., Konzett, J., Lugli, F., Mazzucchelli, M. & Tropper, P. (2020). In situ Sr isotope analysis of mantle carbonates: constraints on the evolution and sources of metasomatic carbon-bearing fluids in a paleo-collisional setting. *Lithos* **354-355**, 105334. https://doi.org/10.1016/j.lithos.2019.105334.

Cook, N. D. J. & Ashley, P. M. (1992). Meta-evaporite sequence, exhalative chemical sediments and associated rocks in the Proterozoic Willyama Supergroup, South Australia: implications for metallogenesis. *Precambrian Research* **56**, 211–226. https://doi.org/10.1016/0301-9268(92)90102-T.

Dahal, R. K. & Adhikary, P. C. (2021). Geology of the Kharidhunga—Thokarpa area, Central Nepal, Lesser Himalaya. *Journal of Nepal Geological Society* **23**, 19–26. https://doi.org/10.3126/jngs.v23i0.31863.

Dasgupta, D. (1993). Contrasting mineral parageneses in high temperature calc-silicate granulites: example from the eastern Ghats, India. *Journal of Metamorphic Geology* **11**, 193–202. https://doi.org/10.1111/j.1525-1314.1993.tb00142.x.

DeCelles, P. G., Gehrels, G. E., Quade, J., Ojha, T. P., Kapp, P. A. & Upreti, B. N. (1998). Neogene foreland basin deposits erosional

unroofing and the kinematic history of the Himalayan fold–thrust belt, western Nepal. *Geological Society of America Bulletin* **110**, 2–21. https://doi.org/10.1130/0016-7606(1998)110%3c0002:NFBDEU%3e2.3.CO;2.

DeCelles, P. G., Gehrels, G. E., Quade, J. & Ojha, T. P. (2000). Eocene–early Miocene foreland basin development and the history of Himalayan thrusting, western and Central Nepal. *Tectonics* **17**, 741–765. https://doi.org/10.1029/98TC02598.

DeCelles, P. G., Robinson, D. M., Quade, J., Ojha, T. P., Garzione, C. N., Copeland, P. & Upreti, B. N. (2001). Stratigraphy, structure and tectonic evolution of the Himalayan fold–thrust belt in western Nepal. *Tectonics* **20**, 487–509. https://doi.org/10.1029/2000TC001226.

Deer, W. A., Howie, R. A. & Zussmann, J. (1992) *An introduction to the rock-forming minerals*, II edn. London: Longman, p.696.

Dhital, M. R. (2015) Geology of Nepal Himalaya. In: Oberhänsli, R., de Wit, M. J. & Roure, F. M., (eds) *Regional perspective of the classic collided orogen. Regional Geology Review*. Springer International Publishing, p.498.

Diener, J. F. A. & Powell, R. (2012). Revised activity–composition models for clinopyroxene and amphibole. *Journal of Metamorphic Geology* **30**, 131–142. https://doi.org/10.1111/j.1525-1314.2011.00959.x.

Diener, J. F. A., Powell, R., White, R. W. & Holland, T. J. B. (2007). A new thermodynamic model for clino- and orthoamphiboles in the system $Na_2O–CaO–FeO–MgO–Al_2O_3–SiO_2–H_2O–O$. *Journal of Metamorphic Geology* **25**, 631–656. https://doi.org/10.1111/j.1525-1314.2007.00720.x.

Diener, J. F. A., Powell, R. & White, R. W. (2008). Quantitative phase petrology of cordierite–orthoamphibole gneisses and related rocks. *Journal of Metamorphic Geology* **26**, 795–814. https://doi.org/10.1111/j.1525-1314.2008.00791.x.

Dong, A., Zhu, X.-K., Li, S.-Z., Kendall, B., Wang, Y. & Gao, Z. (2016). Genesis of a giant Paleoproterozoic stratabound magnesite deposit: constraints from Mg isotopes. *Precambrian Research* **281**, 673–683. https://doi.org/10.1016/j.precamres.2016.06.020.

Eberhard, L. & Pettke, T. (2021). Antigorite dehydration fluids boost carbonate mobilisation and crustal CO_2 outgassing in collisional orogens. *Geochimica et Cosmochimica Acta* **300**, 192–214. https://doi.org/10.1016/j.gca.2021.02.030.

Eugster, H. P. (1985). Oil shales, evaporites and ore deposits. *Geochimica et Cosmochimica Acta* **49**, 619–635. https://doi.org/10.1016/0016-7037(85)90158-9.

Eugster, H. P. & Chou, I.-M. (1973). The depositional environment of Precambrian banded iron formations. *Economic Geology* **68**, 1144–1168. https://doi.org/10.2113/gsecongeo.68.7.1144.

Evans, M. J., Derry, L. A. & France-Lanord, C. (2008). Degassing of metamorphic carbon dioxide from the Nepal Himalaya. *Geochemistry, Geophysics, Geosystems* **9**, Q04021. https://doi.org/10.1029/2007GC001796.

Falk, E. S. & Kelemen, P. B. (2015). Geochemistry and petrology of listvenite in the Samail ophiolite, Sultanate of Oman: complete carbonation of peridotite during ophiolite emplacement. *Geochimica et Cosmochimica Acta* **160**, 70–90. https://doi.org/10.1016/j.gca.2015.03.014.

Faryad, S. W. (2002). Metamorphic conditions and fluid compositions of scapolite-bearing rocks from the Lapis Lazuli deposit at Sare Sang, Afghanistan. *Journal of Petrology* **43**, 725–747. https://doi.org/10.1093/petrology/43.4.725.

Ferrando, S., Groppo, C., Frezzotti, M. L., Castelli, D. & Proyer, A. (2017). Dissolving dolomite in a stable UHP mineral assemblage: evidence from Cal-Dol marbles of the Dora-Maira Massif (Italian Western Alps). *American Mineralogist* **102**, 42–60. https://doi.org/10.2138/am-2017-5761.

Ferry, J. M. (1976). Metamorphism of calcareous sediments in the Waterville–Vassalboro area, south–central Maine: mineral reactions and graphical analysis. *American Journal of Science* **276**, 841–882. https://doi.org/10.2475/ajs.276.7.841.

Ferry, J. M. (1983a). On the control of temperature, fluid composition and reaction progress during metamorphism. *American Journal of Science* **283A**, 201–232.

Ferry, J. M. (1983b). Regional metamorphism of the Vassalboro Formation, south–central Maine, USA: a case study of the role of a fluid in metamorphic petrogenesis. *Journal of the Geological Society of London* **140**, 551–576. https://doi.org/10.1144/gsjgs.140.4.0551.

Ferry, J. M. (1992). Regional metamorphism of the Waits River Formation, eastern Vermont: delineation of a new type of giant metamorphic hydrothermal system. *Journal of Petrology* **33**, 45–94. https://doi.org/10.1093/petrology/33.1.45.

Fitzsimons, I. C. W. & Harley, S. L. (1994). Garnet coronas in scapolite–wollastonite calc-silicates from East Antarctica: the application and limitations of activity corrected grids. *Journal of Metamorphic Geology* **12**, 761–777. https://doi.org/10.1111/j.1525-1314.1994.tb00058.x.

Frank, T. D. & Fielding, C. R. (2003). Marine origin for Precambrian, carbonate-hosted magnesite? *Geology* **31**, 1101–1104. https://doi.org/10.1130/G20101.1.

Frezzotti, M. L., Selverstone, J., Sharp, Z. D. & Compagnoni, R. (2011). Carbonate dissolution during subduction revealed by diamond-bearing rocks from the Alps. *Nature Geoscience* **4**, 703–706. https://doi.org/10.1038/ngeo1246.

Frisch, W., Meschede, M. & Blakey, R. (2011) *Plate Tectonics: Continental Drift and Mountain Building*. Berlin: Springer Berlin Heidelberg, p.212.

Fuhrman, M. L. & Lindsley, D. H. (1988). Ternary-feldspar modeling and thermometry. *American Mineralogist* **73**, 201–215.

Gansser, A. (1964) Geology of the Himalayas. In: De Sitter, L. U. (ed) *Regional Geology Series*. London: Interscience Publishers, John Wiley and Sons, p.289.

Garnier, V., Giuliani, G., Ohnenstetter, D., Fallick, A., Dubessy, J., Banks, D., Quang Vinh, H., Lhomme, T., Maluski, H., Pêcher, A., Allah Bakhsh, K., Van Long, P., Trong Trinh, P. & Schwarz, D. (2008). Marble-hosted ruby deposits from Central and Southeast Asia: towards a new genetic model. *Ore Geology Reviews* **34**, 169–191. https://doi.org/10.1016/j.oregeorev.2008.03.003.

Girault, F., Bollinger, L., Bhattarai, M., Koirala, B. P., France-Lanord, C., Rajaure, S., Gaillardet, J., Fort, M., Sapkota, S. N. & Perrier, F. (2014). Large-scale organization of carbon dioxide discharge in the Nepal Himalayas. *Geophysical Research Letters* **41**, 6358–6366. https://doi.org/10.1002/2014GL060873.

Girault, F., Adhikari, L. B., France-Lanord, C., Agrinier, P., Koirala, B. P., Bhattarai, M., Mahat, S., Groppo, C., Rolfo, F., Bollinger, L. & Perrier, F. (2018). Persistent CO_2 emissions and hydrothermal unrest following the 2015 earthquake in Nepal. *Nature Communications* **9**, 2956. https://doi.org/10.1038/s41467-018-05138-z.

Girault, F., France-Lanord, C., Adhikari, L. B., Upreti, B. N., Paudyal, K. R., Gajurel, A. P., Agrinier, P., Losno, R., Groppo, C., Rolfo, F., Thapa, S., Tamang, S. & Perrier, F. (2023a) Chapter 9: Crustal fluids in the Nepal Himalaya and sensitivity to the earthquake cycle. In: Cattin R. & Epard J.-L. (eds) *Himalaya, Dynamics of a Giant, volume 3*. Wiley: ISTE Ltd., pp. 239–265.

Girault, F., France-Lanord, C., Adhikari, L. B., Upreti, B. N., Paudyal, K. R., Gajurel, A. P., Agrinier, P., Losno, R., Thapa, S., Tamang, S., Mahat, S. S., Bhattarai, M., Koirala, B. P., Gupta, R. M., Maharjan, K., Tamang, N. G., Bouquerel, H., Gaillardet, J., Dellinger, M., Prevot, F.,

Chaduteau, C., Rigaudier, T., Assayag, N. & Perrier, F. (2023b) Chapter 8: Overview of hydrothermal systems in the Nepal Himalaya. In: Cattin R. & Epard J.-L. (eds) *Himalaya, Dynamics of a Giant, volume 1*. ISTE Ltd: Wiley, pp. 225–254.

Giuliani, G., Olivo, G. R., Marini, O. J. & Michel, D. (1993). The Santa Rita gold deposit in the Proterozoic Paranoa Group, Goias, Brazil: an example of fluid mixing during ore deposition. *Ore Geology Reviews* **8**, 503–523. https://doi.org/10.1016/0169-1368(93)90042-W.

Giuliani, G., France-Lanord, C., Cheilletz, A., Coget, P., Branquet, Y. & Laumonier, B. (2000). Sulfate reduction by organic matter in Colombian emerald deposits: chemical and stable isotope (C, O, H) evidence. *Economic Geology* **95**, 1129–1153. https://doi.org/10.2113/95.5.1129.

Godard, G. (2009). Two orogenic cycles in eclogite-facies gneisses of the southern Armorican Massif (France). *European Journal of Mineralogy* **21**, 1173–1190. https://doi.org/10.1127/0935-1221/2009/0021-1984.

Goldsmith, J. R. & Newton, R. C. (1969). P-T-X relations in the system $CaCO_3$-$MgCO_3$ at high temperatures and pressures. *American Journal of Science* **267A**, 160–190.

Greenwood, H. J. (1975). Buffering of pore fluids by metamorphic reactions. *American Journal of Science* **275**, 573–593. https://doi.org/10.2475/ajs.275.5.573.

Gresens, R. L. (1978). Evaporites as precursors of massif anorthosite. *Geology* **6**, 46–50. https://doi.org/10.1130/0091-7613(1978)6%3c46:EAPOMA%3e2.0.CO;2.

Groppo, C., Rolfo, F. & Castelli, D. (2007). Pre-Alpine HT mineral relics in impure marbles from the UHP Brossasco-Isasca Unit (Dora-Maira Massif, western Alps). *Periodico di Mineralogia* **76**, 155–168.

Groppo, C., Rolfo, F. & Lombardo, B. (2009). P-T evolution across the Main Central Thrust Zone (Eastern Nepal): hidden discontinuities revealed by petrology. *Journal of Petrology* **50**, 1149–1180. https://doi.org/10.1093/petrology/egp036.

Groppo, C., Rolfo, F., Castelli, D. & Mosca, P. (2017). Metamorphic CO_2 production in collisional orogens: petrologic constraints from phase diagram modeling of Himalayan, scapolite-bearing, calc-silicate rocks in the NKC(F)MAS(T)–HC system. *Journal of Petrology* **58**, 53–83. https://doi.org/10.1093/petrology/egx005.

Groppo, C., Rapa, G., Frezzotti, M. L. & Rolfo, F. (2021). The fate of calcareous pelites in collisional orogens. *Journal of Metamorphic Geology* **39**, 181–207. https://doi.org/10.1111/jmg.12568.

Groppo, C., Rapa, G., Rolfo, F. & Frezzotti, M. L. (2022). CO_2 outgassing during collisional orogeny is facilitated by the generation of immiscible fluids. *Communications Earth & Environment* **3**, 13. https://doi.org/10.1038/s43247-022-00340-w.

Groppo, C., Rolfo, F., Tamang, S. & Mosca, P. (2023) Chapter 7: Lithostratigraphy, petrography and metamorphism of the Lesser Himalayan Sequence. In: Cattin R. & Epard J.-L. (eds) *Himalaya, Dynamics of a Giant, volume 2*. ISTE Ltd: Wiley, pp. 159–188.

Hansen, L. D., Dipple, G. M., Gordon, T. M. & Kellett, D. A. (2005). Carbonated serpentinite (listwanite) at Atlin, British Columbia: a geological analogue to carbon dioxide sequestration. *Canadian Mineralogist* **43**, 225–239. https://doi.org/10.2113/gscanmin.43.1.225.

Hanson, R. E., Wilson, T. J. & Munyanyiwa, H. (1994). Geologic evolution of the Neoproterozoic Zambezi orogenic belt in Zambia. *Journal of African Earth Sciences* **18**, 135–150. https://doi.org/10.1016/0899-5362(94)90026-4.

Harley, S. L. & Buick, I. S. (1992). Wollastonite–scapolite assemblages as indicators of granulite pressure–temperature–fluid history: the Rauer Group, East Antactica. *Journal of Petrology* **33**, 693–728. https://doi.org/10.1093/petrology/33.3.693.

Haynes, D. W. (1986a). Stratiform copper deposits hosted by low energy sediments: I. Timing of sulfide precipitation - an hypothesis. *Economic Geology* **81**, 250–265. https://doi.org/10.2113/gsecongeo.81.2.250.

Haynes, D. W. (1986b). Stratiform copper deposits hosted by low energy sediments: II. Nature of source rocks and composition of metal-transporting water. *Economic Geology* **81**, 266–280. https://doi.org/10.2113/gsecongeo.81.2.266.

Hewitt, D. A. (1973). The metamorphism of micaceous limestones from south–Central Connecticut. *American Journal of Science* **273A**, 444–469.

Hofer, G., Wagreich, M. & Neuhuber, S. (2013). Geochemistry of fine grained sediments of the upper cretaceous to Paleogene Gosau Group (Austria, Slovakia): Implications for paleoenvironmental and provenance studies. *Geoscience Frontiers* **4**, 449–468. https://doi.org/10.1016/j.gsf.2012.11.009.

Hogarth, D. D. & Griffin, W. L. (1978). Lapis lazuli from Baffin Island—a Precambrian meta-evaporite. *Lithos* **11**, 37–60. https://doi.org/10.1016/0024-4937(78)90030-0.

Holland, T. J. B. & Powell, R. (1998). An internally consistent thermodynamic data set for phases of petrologic interest. *Journal of Metamorphic Geology* **16**, 309–343. https://doi.org/10.1111/j.1525-1314.1998.00140.x.

Holland, T., Baker, J. & Powell, R. (1998). Mixing properties and activity-composition relationships of chlorites in the system MgO-FeO-Al_2O_3-SiO_2-H_2O. *European Journal of Mineralogy* **10**, 395–406. https://doi.org/10.1127/ejm/10/3/0395.

Hu, H., Vitale Brovarone, A., Zhang, L., Piccoli, F., Peng, W. & Shen, T. (2021). Retrograde carbon sequestration in orogenic complexes: a case study from the Chinese southwestern Tianshan. *Lithos* **392-393**, 106151. https://doi.org/10.1016/j.lithos.2021.106151.

Joshi, P. & Sharma, R. (2015). Fluid inclusion and geochemical signatures of the talc deposits in Kanda area, Kumaun, India: implications for genesis of carbonate hosted talc deposits in lesser Himalaya. *Carbonates and Evaporites* **30**, 153–166. https://doi.org/10.1007/s13146-014-0196-3.

Jowett, E. C., Rydzewski, A. & Jowett, R. J. (1987). The Kupferschiefer Cu-Ag ore deposits in Poland: a re-appraisal of the evidence of their origin and presentation of a new genetic model. *Canadian Journal of Earth Sciences* **24**, 2016–2037. https://doi.org/10.1139/e87-192.

Kelemen, P. B. & Manning, C. E. (2015). Reevaluating carbon fluxes in subduction zones, what goes down, mostly comes up. *Proc Natl Acad Sci USA* **112**, E3997–E4006. https://doi.org/10.1073/pnas.1507889112.

Kerrick, D. M. & Caldeira, K. (1998). Metamorphic CO_2 degassing from orogenic belts. *Chemical Geology* **145**, 213–232. https://doi.org/10.1016/S0009-2541(97)00144-7.

Kohn, M. J. (2014). Himalayan metamorphism and its tectonic implications. *Annual Review of Earth and Planetary Sciences* **42**, 381–419. https://doi.org/10.1146/annurev-earth-060313-055005.

Kohn, M. J., Paul, S. K. & Corrie, S. L. (2010). The lower Lesser Himalayan sequence: a Paleoproterozoic arc on the northern margin of the Indian plate. *Geological Society of America Bulletin* **122**, 323–335. https://doi.org/10.1130/B26587.1.

Kucha, H. & Pawlikowski, M. (1986). Two-brine model of the genesis of strata-bound Zechstein deposits (Kupferschiefer type), Poland. *Mineralium Deposita* **21**, 70–80. https://doi.org/10.1007/BF00204365.

Kuhn, B. K., Reusser, E. & Powell, R. (2005). Metamorphic evolution of calc-schists in the Central Alps, Switzerland. *Schweizerische Mineralogische und Petrographische Mitteilungen* **85**, 175–190.

Kulke, H. & Schreyer, W. (1973). Kyanite-talc schist from Sar e Sang, Afghanistan. *Earth and Planetary Science Letters* **18**, 324–328. https://doi.org/10.1016/0012-821X(73)90071-X.

Le Fort, P. & Rai, S. M. (1999). Pre-tertiary felsic magmatism of the Nepal Himalaya: recycling of continental crust. *Journal of Asian Earth Sciences* **17**, 607–628. https://doi.org/10.1016/S1367-9120(99)00015-2.

Leake, B. E. & Farrow, C. M. (1979). A pre-2,000 Myr old granulite facies metamorphosed evaporite from Caraíba, Brazil? *Nature* **277**, 49–50. https://doi.org/10.1038/277049a0.

Long, S. P. & Robinson, D. M. (2021). Construction of the Lesser Himalayan–Subhimalayan thrust belt: the primary driver of thickening, exhumation, and high elevations in the Himalayan orogen since the middle Miocene. *Geology* **49**, 1283–1288. https://doi.org/10.1130/G48967.1.

Maffeis, A., Ferrando, S., Connolly, J. A. D., Groppo, C., Frezzotti, M. L. & Castelli, D. (2021). Thermodynamic analysis of HP-UHP fluid inclusions: the solute load and chemistry of metamorphic fluids. *Geochimica et Cosmochimica Acta* **315**, 207–229. https://doi.org/10.1016/j.gca.2021.08.044.

Martin, A. J., DeCelles, P. G., Gehrels, G. H., Patchett, P. J. & Isachsen, C. (2005). Isotopic and structural constraints on the location of the Main Central Thrust in the Annapurna range, Central Nepal Himalaya. *Geological Society of America Bulletin* **117**, 926–944. https://doi.org/10.1130/B25646.1.

Martin, A. J., Burgya, K. D., Kaufmanb, A. J. & Gehrels, G. E. (2011). Stratigraphic and tectonic implications of field and isotopic constraints on depositional ages of Proterozoic Lesser Himalayan rocks in Central Nepal. *Precambrian Research* **185**, 1–17. https://doi.org/10.1016/j.precamres.2010.11.003.

Massonne, H. J. (2010). Phase relations and dehydration behaviour of calcareous sediments at very-low to low grade metamorphic conditions. *Periodico di Mineralogia* **79**, 21–43.

Mathavan, V. & Fernando, G. W. A. R. (2001). Reactions and textures in grossular–wollastonite–scapolite calc-silicate granulites from Maligawila, Sri Lanka: evidence for high temperature isobaric cooling in the meta-sediments of the Highland complex. *Lithos* **59**, 217–232. https://doi.org/10.1016/S0024-4937(01)00057-3.

McLennan, S. M., Hemming, S., McDaniel, D. K. & Hanson, G. N. (1993) Geochemical approaches to sedimentation, provenance, and tectonics. In: Johnsson M. J. & Basu A. (eds) *Processes Controlling the Composition of Clastic Sediments*, GSA Special Papers, v. 284. Geological Society of America, pp. 21–40.

Menard, T. & Spear, F. S. (1993). Metamorphism of calcic pelitic schists, Strafford Dome, Vermont: compositional zoning and reaction history. *Journal of Petrology* **34**, 977–1005. https://doi.org/10.1093/petrology/34.5.977.

Menzel, M. D., Garrido, C. J., López Sánchez-Vizcaíno, V., Marchesi, C., Hidas, K., Escayola, M. P. & Delgado-Huertas, A. (2018). Carbonation of mantle peridotite by CO2-rich fluids: the formation of listvenites in the advocate ophiolite complex (Newfoundland, Canada). *Lithos* **323**, 238–261. https://doi.org/10.1016/j.lithos.2018.06.001.

Moine, B., Sauvan, P. & Jarousse, J. (1981). Geochemistry of evaporite-bearing series: a tentative guide for the identification of meta-evaporites. *Contributions to Mineralogy and Petrology* **76**, 401–412. https://doi.org/10.1007/BF00371482.

Moore, J. N. & Kerrick, D. M. (1976). Equilibria in siliceous dolomites of the Alta aureole, Utah. *American Journal of Science* **276**, 502–524. https://doi.org/10.2475/ajs.276.4.502.

Moore, J. M. & Waters, D. J. (1990). Geochemistry and origin of cordierite–orthoamphibole/orthopyroxene–phlogopite rocks from Namaqualand, South Africa. *Chemical Geology* **85**, 77–100. https://doi.org/10.1016/0009-2541(90)90124-P.

Morissey, L. J. & Tomkins, A. G. (2020). Evaporite-bearing orogenic belts produce ligand-rich and diverse metamorphic fluids. *Geochimica et Cosmochimica Acta* **275**, 163–187. https://doi.org/10.1016/j.gca.2020.02.017.

Neudert, M. K. & Russell, R. E. (1981). Shallow water and hypersaline features from the middle Proterozoic Mt. Isa sequence. *Nature* **293**, 284–286.

Oliver, N. H. S. (1995). Hydrothermal history of the Mary Kathleen fold belt, Mt Isa Block, Queensland. *Australian Journal of Earth Sciences* **42**, 267–279. https://doi.org/10.1080/08120099508728201.

Ortega-Gutierrez, F. (1984). Evidence of Precambrian evaporates in the Oaxacan granulite complex of southern Mexico. *Precambrian Research* **23**, 377–393. https://doi.org/10.1016/0301-9268(84)90051-2.

Pan, Y. & Fleet, M. E. (1995). Geochemistry and origin of cordierite–orthoamphibole gneiss and associated rocks at an Archaean volcanogenic massive sulphide camp: Manitouwadge, Ontario, Canada. *Precambrian Research* **74**, 73–89. https://doi.org/10.1016/0301-9268(95)00010-3.

Parrish, R. R. & Hodges, K. V. (1996). Isotopic constraints on the age and provenance of the lesser Himalaya. *Geological Society of America Bulletin* **108**, 904–911. https://doi.org/10.1130/0016-7606(1996)108%3c0904:ICOTAA%3e2.3.CO;2.

Pearson, O. N. & DeCelles, P. G. (2005). Structural geology and regional tectonic significance of the Ramgarh thrust, Himalayan fold-thrust belt of Nepal. *Tectonics* **24**, TC4008. https://doi.org/10.1029/2003TC001617.

Pêcher, A. (1989). The metamorphism in central Himalaya. *Journal of Metamorphic Geology* **7**, 31–41. https://doi.org/10.1111/j.1525-1314.1989.tb00573.x.

Peck, W. H. & Eppich, G. R. (2019). The Kilmar magnesite deposits: evaporitic Metasediments in the Grenville Supergroup, Morin terrane, Quebec. *Minerals* **9**, 554. https://doi.org/10.3390/min9090554.

Peck, W. H. & Smith, M. S. (2005). Cordierite–gedrite rocks from the Central Metasedimentary Belt boundary thrust zone (Grenville Province, Ontario): Mesoproterozoic metavolcanic rocks with affinities to the Composite Arc Belt. *Canadian Journal of Earth Sciences* **42**, 1815–1828. https://doi.org/10.1139/e05-071.

Plank, T. & Manning, C. E. (2019). Subducting carbon. *Nature* **574**, 343–352. https://doi.org/10.1038/s41586-019-1643-z.

Pohl, W. (1990). Genesis of magnesite deposits—models and trends. *Geologische Rundschau* **79**, 291–299. https://doi.org/10.1007/BF01830626.

Poli, S. (2015). Carbon mobilized at shallow depths in subduction zones by carbonatitic liquids. *Nature Geoscience* **8**, 633–636. https://doi.org/10.1038/ngeo2464.

Pouchou, J. L. & Pichoir, F. (1988) Determination of mass absorption coefficients for soft X-rays by use of the electron microprobe. In: Newbury D. E. (ed) *Microbeam Analysis*. San Francisco, CA: San Francisco Press, pp. 319–324.

Prochaska, W. & Krupenin, M. (2013). Formation of magnesite and siderite deposits in the southern Urals—evidence of inclusion fluid chemistry. *Mineralogy and Petrology* **107**, 53–65. https://doi.org/10.1007/s00710-012-0251-5.

Proyer, A., Mposkos, E., Baziotis, I. & Hoinkes, G. (2008). Tracing high-pressure metamorphism in marbles: phase relations in high-grade aluminous calcite-dolomite marbles from the Greek Rhodope massif in the system CaO-MgO-Al$_2$O$_3$-SiO$_2$-CO$_2$ and indications of prior aragonite. *Lithos* **104**, 119–130. https://doi.org/10.1016/j.lithos.2007.12.002.

Rapa, G., Groppo, C., Mosca, P. & Rolfo, F. (2016). Petrological constraints on the tectonic setting of the Kathmandu Nappe in the Langtang–Gosainkund–Helambu regions, Central Nepal Himalaya. *Journal of Metamorphic Geology* **34**, 999–1023. https://doi.org/10.1111/jmg.12219.

Rapa, G., Groppo, C., Rolfo, F., Petrelli, M., Mosca, P. & Perugini, D. (2017). Titanite-bearing calc-silicate rocks constrain timing, duration, and magnitude of metamorphic CO_2 degassing in the Himalayan belt. *Lithos* **292-293**, 364–378. https://doi.org/10.1016/j.lithos.2017.09.024.

Reinhardht, J. (1987). Cordierite-anthophyllite rocks from north-west Queensland, Australia: metamorphosed magnesian pelites. *Journal of Metamorphic Geology* **5**, 451–472. https://doi.org/10.1111/j.1525-1314.1987.tb00396.x.

Rice, J. M. (1977a). Progressive metamorphism of impure dolomitic limestone in the Marysville aureole, Montana. *American Journal of Science* **277**, 1–24. https://doi.org/10.2475/ajs.277.1.1.

Rice, J. M. (1977b). Contact metamorphism of impure dolomitic limestone in the Boulder Aureole, Montana. *Contributions to Mineralogy and Petrology* **59**, 237–259. https://doi.org/10.1007/BF00374555.

Rich, R. A. (1979). Fluid inclusion evidence of Silurian evaporites in southeastern Vermont. *Geological Society of America Bulletin* **90**, 1628–1643. https://doi.org/10.1130/GSAB-P2-90-1628.

Roberts, M. D., Oliver, N. H. S., Fairclough, M. C., Hölttä, P. S. & Lahtinen, R. (2003). Geochemical and oxygen isotope signature of sea-floor alteration associated with a polydeformed and highly metamorphosed massive sulphide deposit, Ruostesuo, Central Finland. *Economic Geology* **98**, 535–556.

Rolfo, F., Groppo, C. & Mosca, P. (2017). Metamorphic CO_2 production in calcsilicate rocks from the eastern Himalaya. *Italian Journal of Geosciences* **136**, 28–23. https://doi.org/10.3301/IJG.2015.36.

Sakai, H., Iwano, H., Danhara, T., Takigami, Y., Rai, S. M., Upreti, B. N. & Hirata, T. (2013). Rift-related origin of the Paleoproterozoic Kuncha formation, and cooling history of the Kuncha nappe and Taplejung granites, eastern Nepal Lesser Himalaya: a multichronological approach. *Island Arc* **22**, 338–360. https://doi.org/10.1111/iar.12021.

Schmädicke, E., Okrusch, M., Schubert, W., Elwart, B. & Görke, U. (2001). Phase relations of calc-silicate assemblages in the Auerbach marble, Odenwald crystalline complex, Germany. *Mineralogy and Petrology* **72**, 77–111. https://doi.org/10.1007/s007100170028.

Schryer, W. & Abraham, K. (1976). Three-stage metamorphic history of a whiteschist from Sar e Sang, Afghanistan, as part of a former evaporite deposit. *Contributions to Mineralogy and Petrology* **59**, 111–130. https://doi.org/10.1007/BF00371302.

Sengupta, P. & Raith, M. M. (2002). Garnet stoichiometry as petrogenetic indicator: an example from the marble–calcsilicate interface from Kondapalle, Eastern Ghats Belt. *American Journal of Science* **302**, 686–725. https://doi.org/10.2475/ajs.302.8.686.

Sengupta, P., Sanyal, S., Dasgupta, S., Fukuoka, M. & Ehl, J. (1997). Controls of mineral reactions in high-grade garnet–wollastonite–scapolite-bearing calcsilicate rocks: an example from Anakapalle, Eastern Ghats, India. *Journal of Metamorphic Geology* **15**, 551–564. https://doi.org/10.1111/j.1525-1314.1997.tb00635.x.

Sieber, M. J., Hermann, J. & Yaxley, G. M. (2018). An experimental investigation of C–O–H fluid-driven carbonation of serpentinites under forearc conditions. *Earth and Planetary Science Letters* **496**, 178–188. https://doi.org/10.1016/j.epsl.2018.05.027.

Skippen, G. B. (1971). Experimental data for reactions in siliceous marbles. *Journal of Geology* **79**, 457–481. https://doi.org/10.1086/627652.

Skippen, G. B. (1974). An experimental model for low pressure metamorphism of siliceous dolomitic marble. *American Journal of Science* **274**, 487–509. https://doi.org/10.2475/ajs.274.5.487.

Skippen, G. B. & Hutcheon, I. (1974). The experimental calibration of continuous reactions in siliceous carbonate rocks. *Canadian Mineralogist* **12**, 327–333.

Smith, M. S., Dymek, R. F. & Schneiderman, J. S. (1992). Implications of trace element geochemistry for the origin of cordierite–anthophyllite rocks from Orijärvi, SW Finland. *Journal of Geology* **100**, 545–559. https://doi.org/10.1086/629607.

Stephenson, N. C. N. & Cook, N. D. J. (1997). Metamorphic evolution of calcsilicate granulites near Battye Glacier, northern Prince Charles Mountains, East Antarctica. *Journal of Metamorphic Geology* **15**, 361–378. https://doi.org/10.1111/j.1525-1314.1997.00024.x.

Stewart, E. M., Ague, J. J., Ferry, J. M., Schiffries, C. M., Tao, R.-B., Isson, T. T. & Planavsky, N. J. (2019). Carbonation and decarbonation reactions: implications for planetary habitability. *American Mineralogist* **104**, 1369–1380. https://doi.org/10.2138/am-2019-6884.

Stöcklin, J. (1980). Geology of Nepal and its regional frame. *Journal of the Geological Society of London* **137**, 1–34. https://doi.org/10.1144/gsjgs.137.1.0001.

Svenningsen, O. (1994). Tectonic significance of the meta-evaporite magnesite and scapolite deposits in the seve-nappes, Sarek Mts, Swedish Caledonides. *Tectonophysics* **231**, 33–44. https://doi.org/10.1016/0040-1951(94)90119-8.

Tamang, S., Groppo, C., Girault, F. & Rolfo, F. (2023). Implications of garnet nucleation overstepping for the P-T evolution of the Lesser Himalayan Sequence of Central Nepal. *Journal of Metamorphic Geology* **41**, 271–297. https://doi.org/10.1111/jmg.12695.

Thapa, S., Girault, F., Deldicque, D., Losno, R., France-Lanord, C., Groppo, C., Rolfo, F., Tamang, S., Rigaudier, T., Debret, B., Paudyal, K. R., Adhikari, L. B. & Perrier, F. (2023). Metric, kilometric and large-scale coherence of metamorphic conditions from graphitic phyllite in the Upper Lesser Himalaya of Nepal: contribution to the estimation of carbon stored during Himalayan orogeny. *Chemical Geology* **623**, 121378. https://doi.org/10.1016/j.chemgeo.2023.121378.

Thompson, A. B. (1975). Mineral reactions in a calc-mica schist from Gassetts, Vermont, U.S.A. *Contribution to Mineralogy and Petrology* **53**, 105–127. https://doi.org/10.1007/BF00373126.

Thomson, A. R., Walter, M. J., Kohn, S. C. & Brooker, R. A. (2016). Slab melting as a barrier to deep carbon subduction. *Nature* **529**, 76–79. https://doi.org/10.1038/nature16174.

Torres, R. R. L. (1978). Scapolite-bearing and related calcsilicate layers from the Alpujarride Series, (Betic Cordilleras of southern Spain): a discussion on their origin and some comments. *Geologische Rundschau* **67**, 342–355. https://doi.org/10.1007/BF01803272.

Ulmer, P. (1986) *NORM - Program for Cation and Oxygen Mineral Norms*. Zürich: Computer Library IKP-ETH.

Upreti, B. N. (1999). An overview of the stratigraphy and tectonics of the Nepal Himalaya. *Journal of Asian Earth Sciences* **17**, 577–606. https://doi.org/10.1016/S1367-9120(99)00047-4.

Valdiya, K. S. (1995). Proterozoic sedimentation and Pan-African geodynamic development in the Himalaya. *Precambrian Research* **74**, 35–55. https://doi.org/10.1016/0301-9268(95)00004-O.

Walker, R. N., Muir, M. D., Diver, W. L., Williams, N. & Wilkins, N. (1977). Evidence of major sulphate evaporate deposits in the Proterozoic McArthur group, Northern Territory, Australia. *Nature* **265**, 526–529. https://doi.org/10.1038/265526a0.

Warren, J. K. (1997). Evaporites, brines and base metals: fluids, flow and "the evaporite that was". *Australian Journal of Earth Sciences* **44**, 149–183. https://doi.org/10.1080/08120099708728302.

White, R. W., Powell, R. & Holland, T. J. B. (2007). Progress relating to calculation of partial melting equilibria for metapelites. *Journal of Metamorphic Geology* **25**, 511–527. https://doi.org/10.1111/j.1525-1314.2007.00711.x.

White, R. W., Powell, R. & Johnson, T. E. (2014). The effect of Mn on mineral stability in metapelites revisited: new a–x relations for manganese-bearing minerals. *Journal of Metamorphic Geology* **32**, 809–828. https://doi.org/10.1111/jmg.12095.

Whitney, D. L. & Evans, B. W. (2010). Abbreviations for names of rock-forming minerals. *American Mineralogist* **95**, 185–187. https://doi.org/10.2138/am.2010.3371.

Yardley, B. W. D. (1997). *The evolution of fluids through the metamorphic cycle*. In: Jamtveit B. & Yardley B. W. D. (eds.) *Fluid Flow and Transport in Rocks*. Dordrecht: Springer, pp. 99–121, https://doi.org/10.1007/978-94-009-1533-6_6.

Yavuz, F. (2007). WinAmphcal: a windows program for the IMA-04 amphibole classification. *Geochemistry, Geophysics, Geosystems* **8**, Q01004. https://doi.org/10.1029/2006GC001391.

Yin, A. & Harrison, T. M. (2000). Geologic evolution of the Himalayan-Tibetan orogen. *Annual Review of Earth and Planetary Sciences* **28**, 211–280. https://doi.org/10.1146/annurev.earth.28.1.211.

Zen, E. (1981) A study of progressive regional metamorphism of pelitic schists from the Taconic allochthon of southwestern Massachusetts and its bearing on the geologic history of the area. *US Geological Survey Professional Paper 1113*. Washington DC: US Government Printing Office, 128 pp.